Regional-scale stratigraphy of surface units in Tyrrhena and Iapygia Terrae, Mars: Insights into highland crustal evolution and alteration history

A. Deanne Rogers[1] and Robin L. Fergason[2]

Received 3 November 2010; revised 15 February 2011; accepted 23 May 2011; published 20 August 2011.

[1] The compositional, thermophysical and geologic characteristics of surface units in Iapygia and Tyrrhena Terra (60°E–100°E, 0°–30°S) provide new insights into the compositional stratigraphy of the region. Intercrater plains are dominated by two surface units. The older unit (unit 1) is deficient in olivine and more degraded and likely consists of a mixture of impact, volcanic and sedimentary materials. The younger unit (unit 2) is enriched in olivine, exhibits a resistant morphology and higher thermal inertia, and likely represents volcanic infilling of plains. Units 1 and 2 bear a strong resemblance to those previously mapped in Mare Serpentis, a section of highlands crust located northwest of Hellas Basin. Thus, the two major intercrater plains units are even more widespread than previously thought and therefore likely constitute important components of Mars' highland stratigraphy. Many craters in the region contain high thermal inertia deposits (unit 3) that are compositionally identical to unit 2. These may have formed via volcanic infilling or may represent sedimentary materials that have been eroded from crater walls and lithified. Less common units include olivine and/or pyroxene-rich massifs and crater central peaks. These are primarily found within Hellas Basin rim units and may represent mantle materials brought toward the surface during the Hellas impact. Putative chloride deposits are primarily associated with olivine-deficient surfaces (unit 1) that may be heavily degraded occurrences of unit 2. The observations raise a variety of questions related to Martian crustal evolution and alteration that may have more widespread implications outside the study region.

Citation: Rogers, A. D., and R. L. Fergason (2011), Regional-scale stratigraphy of surface units in Tyrrhena and Iapygia Terrae, Mars: Insights into highland crustal evolution and alteration history, *J. Geophys. Res.*, *116*, E08005, doi:10.1029/2010JE003772.

1. Introduction

[2] Decades of observation have shown that the early history of Mars was rich in geologic activity, including volcanic, aqueous, impact and aeolian processes. Data returned from high-resolution spectrometers show that the surface is spectrally diverse at global, regional and local scales. Local-scale studies of mineral detections and bulk compositional variations whose aims are toward understanding their formation environments and history are numerous and informative [see, e.g., *Christensen et al.*, 2008; *Murchie et al.*, 2009, and references therein]; however, few studies have tried to integrate high-resolution compositional and stratigraphic information at a regional scale. To better understand the volcanic, sedimentary, and impact stratigraphy of the southern highlands, we completed a comprehensive, regional-scale study of surface units in an area that may represent typical highland terrain: the adjoining Tyrrhena and Iapygia Terrae regions (60°E–100°E, 0°–30°S).

[3] This area was chosen as the focus of this study because it includes a large range of spectral and morphologic units that are found throughout the highlands and includes both Noachian and Hesperian age surfaces. First, a variety of local-scale spectral units and spectral unit suites have been identified throughout the southern highlands with Mars Odyssey Thermal Emission Imaging System [*Christensen et al.*, 2004] (THEMIS) multispectral data. These include olivine-rich buttes, olivine/pyroxene-enriched intercrater plain surfaces, olivine-deficient plains, high-silica surfaces, and probable chloride-bearing deposits [e.g., *Bandfield*, 2008; *Bandfield and Rogers*, 2008; *Koeppen and Hamilton*, 2008; *Osterloo et al.*, 2008; *Rogers et al.*, 2009]. Nearly all of the spectral unit types that are commonly observed in the highlands are found within the Iapygia/Tyrrhena Terra region. Additionally, the region contains both Noachian age cratered and dissected plains and Hesperian age smooth units [*Greeley and Guest*, 1987] and also has a diverse set of morphologic features including scarps, massifs, and high thermal inertia (rocky) exposures. Finally, numerous identifications of hydrated silicate minerals have been reported using Mars Reconnais-

[1]Department of Geosciences, State University of New York at Stony Brook, Stony Brook, New York, USA.
[2]U.S. Geological Survey, Flagstaff, Arizona, USA.

0148-0227/11/2010JE003772

sance Orbiter Compact Reconnaissance Imaging Spectrometer for Mars [*Murchie et al.*, 2007] (CRISM) and Mars Express Observatoire pour la Minéralogie, l'Eau, les Glaces et l'Activité [e.g., *Bibring et al.*, 2005] (OMEGA) data. The most areally extensive units are located in Mawrth Vallis and in Nili Fossae; however, many are found in the Noachian highlands, including the Iapygia and Tyrrhena Terra region [e.g., *Mustard et al.*, 2008]. Characterizing the bulk composition of the region provides a geologic and compositional framework for interpreting hydrated silicate detections.

[4] We focused on characterizing the composition, thermophysical properties, local context and geomorphology of THEMIS spectral units in an effort to interpret their possible origin. In order to identify significant events and/or geologic processes that have been dominant in the region, we also characterized the regional context, extent, and geologic variability within these units as well as the stratigraphic relationships between units. The observations were then used to formulate a possible sequence of events. Finally, we present a discussion of outstanding questions related to major THEMIS signatures in the highlands, based on observations presented here and elsewhere.

2. Data and Methods

[5] The THEMIS instrument consists of a 5-band visible imager covering the spectral range between 0.43 and 0.86 μm, and a multispectral thermal infrared imager covering ~6.78–14.88 μm in nine separate channels. The nominal spatial resolutions of each sensor are ~18 m/pixel and ~100 m/pixel, respectively. THEMIS visible images were used for morphologic and relative albedo assessments. THEMIS infrared images were used for analysis of spectral/compositional variability and thermophysical properties. In general, THEMIS daytime radiance and decorrelation stretch (DCS) mosaics were first used to survey the region and get a preliminary picture of surface units in the region. Units were subdivided on the basis of spectral properties and morphology at the km/pixel scale. Each spectral unit was then further characterized using (1) THEMIS thermal inertia, (2) high-resolution visible imagery from THEMIS, Mars Global Surveyor Mars Orbiter Camera (MOC) (1.5–20 m/pixel) [*Malin and Edgett*, 2001], and Mars Reconnaissance Orbiter Context Camera (CTX) (~6 m/pixel) [*Malin et al.*, 2007] images, (3) hyperspectral data from Mars Global Surveyor Thermal Emission Spectrometer (TES) [*Christensen et al.*, 2001], (4) CRISM multispectral survey summary parameter images (~230 m/pixel) [*Seelos et al.*, 2007], and (5) topographic information from the Mars Orbiter Laser Altimeter (MOLA, data binned at 128 pixels per degree) [*D. E. Smith et al.*, 2001] and from the High-Resolution Stereo Camera (HRSC, nominal resolution of 10 m/pixel) [*Jaumann et al.*, 2007].

2.1. THEMIS Multispectral Data

[6] Daytime radiance mosaics for all bands were created for ~5 to 10° square regions within the study area. These mosaics were then decorrelation stretched (DCS) [*Gillespie et al.*, 1986] to highlight spectral variability in the region. The band combination found to exhibit the most variability for this study region is bands 8, 7, and 5 displayed as red, green and blue, respectively; all DCS mosaics (a total of 14) were produced using this band combination. It should be noted that unit color in DCS images depends on spectral variability within the scene. Thus, to quantify the spectral differences between units highlighted by the DCS mosaics, surface emissivity spectra were retrieved from units of interest using the methods of *Bandfield et al.* [2004]. Unit color in DCS images cannot necessarily be used as a proxy for similar compositions across all regions of Mars; only as indicators of relative changes in composition within a scene. However, because many of the surface units identified in this study are present throughout the study region, the DCS color associations tend to be a constant indicator of composition in this work. Mineralogical abundances for spectral units identified with THEMIS were determined using TES data (section 2.3).

2.2. THEMIS Thermal Inertia

[7] To assess thermophysical properties and morphologic variations, THEMIS band 9 daytime radiance mosaics and THEMIS thermal inertia mosaics were used. Thermal inertia is defined as $I = (k\rho c)^{1/2}$, where k is the thermal conductivity, ρ is the bulk density of the surface material, and c is the specific heat, and represents the resistance to change in temperature of the upper few centimeters of the surface throughout the day. Fine particles have a lower thermal inertia, whereas higher thermal inertia surfaces are composed of sand, duricrust, rock fragments, exposed bedrock or a combination of these materials. Many equally plausible scenarios, such as mixtures of particles or the presence of duricrust, can result in surfaces with moderate thermal inertias and therefore additional data sets, such as high resolution visible images, are used to further constrain the surface characteristics. In this study, thermal inertia was particularly useful for constraining the degree of variability in surface properties within each unit, and also comparing and contrasting the physical properties between different units in the study region.

[8] In this work, there were many separate locations classified as the same unit based on spectral and/or morphologic properties. To understand both the typical physical properties of each unit (5 units in total) and how these properties vary within each unit, we sampled images within each unit across the study area. We derived thermal inertia values for 12 THEMIS images per unit with the exception of unit 5 where we choose 1–2 images per instance. Images used in this study were acquired primarily during seasons with a heliocentric longitude of 150° to 325° to ensure warm surfaces with high signal-to-noise ratio. The method of *Fergason et al.* [2006a] was used to derive thermal inertia values from THEMIS nighttime temperature data. Nighttime temperatures only were used because the effects of albedo and Sun-heated slopes have mostly dissipated throughout the night, and the thermal contrast due to differences in particle sizes are at a maximum [e.g., *Kieffer et al.*, 1973, 1977; *Jakosky*, 1979; *Palluconi and Kieffer*, 1981].

[9] The THEMIS nighttime temperatures were converted to a thermal inertia by interpolation within a 7-dimensional look-up table using latitude, season, local solar time, atmospheric dust opacity, thermal inertia, elevation (atmospheric pressure), and albedo as input parameters. This look-up table was generated using a thermal model developed by H. H. Kieffer, which was derived from the Viking

Table 1. Spectral Library[a]

Reference Number	Spectrum Label	Mineral Group
ASU	Quartz BUR-4120	Quartz
ASU	Microcline BUR-3460	Alkali feldspar
ASU	Albite WAR-0235	Plagioclase
ASU	Oligoclase BUR-060D	Plagioclase
ASU	Andesine WAR-0024	Plagioclase
ASU	Labradorite BUR-3080A	Plagioclase
ASU	Bytownite WAR-1384	Plagioclase
ASU	Anorthite BUR-340	Plagioclase
1	Shocked anorthosite	Plagioclase
	at 17 GPa	Plagioclase
	at 21 GPa	Plagioclase
	at 25.5 GPa	Plagioclase
	at 27 GPa	Plagioclase
	at 38 GPa	Plagioclase
	at 56.3 GPa	Plagioclase
ASU	Bronzite NMNH-93527	Orthopyroxene
ASU	Enstatite HS-9.4B	Orthopyroxene
ASU	Hypersthene NMNH-B18247	Orthopyroxene
2	Average Lindsley pigeonite	Low-Ca clinopyroxene
ASU	Diopside WAR-6474	High-Ca clinopyroxene
ASU	Augite NMNH-9780	High-Ca clinopyroxene
ASU	Augite NMHN-122302	High-Ca clinopyroxene
ASU	Hedenbergite manganoan DSM-HED01	High-Ca clinopyroxene
ASU	Forsterite BUR-3720A	Olivine
ASU	Fayalite WAR-RGFAY01	Olivine
3	KI 3362 Fo60	Olivine
3	KI 3115 Fo68	Olivine
3	KI 3373 Fo35	Olivine
3	KI 3008 Fo10	Olivine
4	Illite Imt-1 < 0.2 μm (pellet)	Phyllosilicates
ASU	Ca-montmorillonite solid STx-1	Phyllosilicates
5	Saponite (Eb-1) < 0.2 μm (pellet)	Phyllosilicates
4	SWy-1 < 0.2 microns (pellet)	Phyllosilicates
6	K-rich glass	Glass
6	SiO_2 glass	Glass
7	Opal-A (01–011)	Amorphous silica
8	Al-Opal	Amorphous silica
9	Average Meridiani and Aram Hematite (TT derived)	Oxide
ASU	Anhydrite ML-S9	Sulfate
ASU	Gypsum ML-S6	Sulfate
10	Kieserite	Carbonate
ASU	Calcite C40	Carbonate
ASU	Dolomite C20	Zeolite
11	Crystalline heulandite	Zeolite
11	Crystalline stilbite	Zeolite

[a]Mineral spectra are from the ASU spectral library available online at http://tes.asu.edu [*Christensen et al.*, 2000], except as indicated as alternate sources: (1) *Johnson et al.* [2002]; (2) *Wyatt et al.* [2001]; (3) *Koeppen and Hamilton* [2008]; (4) *Michalski et al.* [2006]; (5) *Michalski et al.* [2005]; (6) *Wyatt et al.* [2001]; (7) *Michalski et al.* [2003]; (8) provided by M. D. Kraft; (9) *Glotch et al.* [2004]; (10) *Baldridge* [2007]; (11) *Ruff* [2004].

IRTM thermal model [*Kieffer et al.*, 1977] with several modifications since then, the most significant being an improved atmospheric component and the ability to model radiatively coupled local slopes at any azimuth (H. H. Kieffer, personal communication, 2010). Model parameters appropriate for the THEMIS image and the measured nighttime surface temperatures were then used to interpolate the thermal inertia between these calculated look-up table node values. Interpolation was performed on a pixel-by-pixel basis using season, latitude, and local solar time from the spacecraft ephemeris. The remaining model input parameters were obtained from external data sets. The albedo of features in the THEMIS image was determined from TES albedo data binned at 8 pixels per degree [*Christensen et al.*, 2001]. Elevation information was ascertained from Mars Orbiter Laser Altimeter (MOLA) data [*Zuber et al.*, 1992; *Smith et al.*, 1999; *D. E. Smith et al.*, 2001] binned at 128 elements per degree. Finally, the opacity was approximated by using a TES-derived climatological database, in which average opacity values for a given set of geographic coordinates and season are stored [e.g., *M. D. Smith et al.*, 2001]. The relative accuracy of THEMIS-derived thermal inertia is ~20% (for additional detail, see *Fergason et al.* [2006a]).

2.3. TES Spectral Data

[10] The TES instrument was part of the Mars Global Surveyor mission, which ended in 2006. The TES instrument consisted of three components: (1) a visible bolometer measuring total solar reflectance between 0.3 and 2.9 μm, (2) a thermal bolometer measuring thermal infrared radiance between 5.1 and 150 μm, and (3) a Michelson interferometer measuring spectral radiance between 5.8 and 50 cm^{-1} at a selectable spectral sampling of 5 or 10 cm^{-1} [*Christensen et al.*, 2001]. Bolometer measurements were used to obtain albedo and thermophysical characteristics of the surface, whereas the hyperspectral data were used to determine compositional and particle size properties of the surface and atmosphere. Atmospheric contributions to TES emissivity spectra were removed by first fitting each spectrum with a library of mineral spectra (Table 1) and atmospheric end-members [*Bandfield et al.*, 2000a] using a linear least squares minimization routine [e.g., *Smith et al.*, 2000; *Bandfield*, 2002]. Atmospheric components were then scaled by their modeled concentrations and subtracted from the measured spectrum to produce surface emissivity. Output from the least squares model also yields an estimate of mineral abundance. For each surface unit identified from THEMIS DCS mosaics, TES spectra were extracted from several occurrences of each unit, and atmospherically corrected. TES spectra were used to estimate the average surface composition for each unit as well as the typical spectral emissivity properties of each unit.

[11] TES spectral indices designed to map the strength of particular spectral features were also used to determine spatial variations in composition. Spectral indices highlight variations in composition without depending on atmospheric correction and spectral modeling methods. The drawback is that absolute values of mineral abundance cannot be determined from spectral index mapping alone. In this work, three TES spectral indices were used. The first two were previously described and validated by *Ruff and Christensen* [2007]. The 465 cm^{-1} index maps the strength of the slope between ~497–508 cm^{-1} and ~466–476 cm^{-1}. As described by *Ruff and Christensen* [2007], 465 cm^{-1} index values are high for surfaces containing elevated abundances of hematite and/or amorphous/poorly crystalline high-silica phases such as obsidian glass, amorphous secondary silica or hydrated silica, zeolites, and some clays. The 530 cm^{-1} index maps the strength of the slope between ~561 cm^{-1} and ~518–529 cm^{-1}. Index values are high for surfaces containing elevated abundances of olivine and/or aluminous dioctahedral smectite clays. Ferric dioctahedral smectites show weaker 530 cm^{-1} index values. A third spectral index,

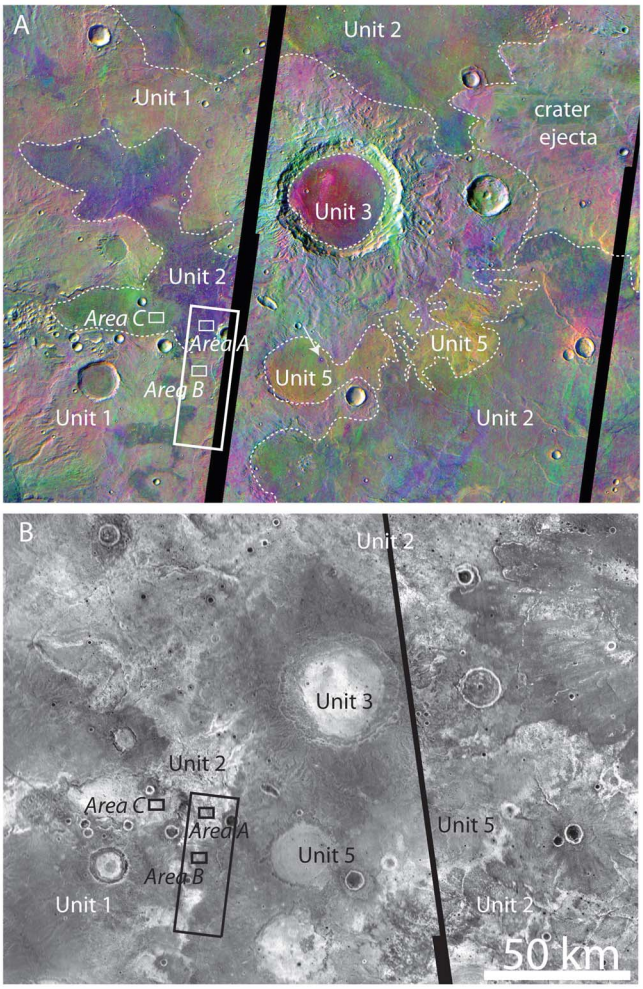

Figure 1. Type localities of units 1, 2, 3 and 5, centered at 62.2°E, 13.4°S, showing typical appearances in THEMIS DCS 8-7-5 images, nighttime radiance, and spatial relationships. (a) THEMIS DCS radiance mosaic using bands 8-7-5 displayed as red, green and blue. Solid line shows location of THEMIS visible image shown in Figure 5. Small white boxes mark locations of THEMIS spectra shown in Figure 7. White arrow points to crater ejecta within unit 5 that is spectrally similar to the underlying unit 2. (b) THEMIS nighttime radiance mosaic.

referred to as the "507 cm^{-1} index," was developed in the course of this work. The 507 cm^{-1} index maps the emissivity slope between 423 and 434 cm^{-1} and 497–508 cm^{-1} (TES channels 27–28 and 34–35). As described in section 3.1, the slope of this feature is affected by the abundance of olivine and/or pyroxene on the surface, relative to plagioclase or high-silica phases.

2.4. CRISM Multispectral Survey Summary Parameter Maps

[12] The CRISM project produces summary parameter maps (~230 m/pixel) from the multispectral survey data (72 channels, 100–200 m/pixel) that map the strength of spectral features associated with various Fe- and OH-bearing minerals [*Seelos et al.*, 2007]. CRISM multispectral survey data were used to search for spatially contiguous concentrations of olivine, pyroxene, and hydrated minerals that might be commonly associated with each unit.

3. Results

[13] Five major surface units were identified in the region, on the basis of spectral properties and geomorphology. Intercrater plains surfaces are divided into units 1 and 2, which are primarily distinguished from each other by their olivine contents and resistant morphology in THEMIS data. Unit 3 is spectrally and morphologically undistinguished from unit 2, but occurs in crater floors rather than intercrater plains. Unit 4 represents intracrater sand deposits found within the region and is spectrally intermediate between unit 1 and units 2–3. Unit 5 is distinguished from units 1–4 primarily by its THEMIS spectral properties and is found associated with a variety of morphologic features. Rare and/or small-scale units are also observed in THEMIS and TES data and are described in section 3.6, but they are not considered major surface units. The area shown in Figure 1 captures four of the five major spectral units present in the study region. The average TES surface emissivity for the five major units are shown in Figure 2, and typical THEMIS surface emissivity for the units are shown in Figure 3. Figure 4 displays derived major mineral abundances (olivine, pyroxene, feldspar and high-silica phases) for individual occurrences of each unit. Feldspar and high-silica phases were combined in Figure 4, because when plotted individually they were not found to vary systematically between units. Conversely, olivine and pyroxene are split from each other because olivine appears to vary between units in more of a systematic manner than pyroxene. Table 2 describes the compositional, thermophysical and geologic properties of each unit, as well as the number of occurrences used to derive the scatterplots in Figure 4 and the spectral averages in Figure 3.

3.1. Unit 1: Olivine-Deficient Intercrater Plains

[14] Degraded intercrater plains surfaces in the study region (Figure 1) are deficient in olivine relative to higher thermal inertia, resistant intercrater plains (unit 2) (Table 2 and Figure 4). There is some variability observed in the strength of the TES 465 cm^{-1} index within this unit, suggesting that high-silica phase abundance is variable. The variations in 465 cm^{-1} index do not correspond to any geomorphic boundaries within the olivine-deficient intercrater plains. Unit 1 typically appears pink or green in DCS 8-7-5 images. Numerous instances of crater ejecta are spectrally indistinguishable from unit 1 (Figure 1); however, there are cases where crater ejecta exhibit higher TES 465 cm^{-1} index values (section 3.6) [see also *Rogers*, 2011].

[15] The plains appear dissected in some areas and lack the resistant morphology (Figure 5) and higher thermal inertia characteristics of the olivine-enriched units. These surfaces form the most extensive and oldest unit in the region and likely include material formed from impact, volcanic, and sedimentary processes [e.g., *Malin*, 1976; *Tanaka et al.*, 1988].

[16] The thermal inertia of this unit is consistent throughout the study area, typically uniform, and ranges from 200 to 380 J m^{-2} K^{-1} $s^{-1/2}$, suggesting a surface that is moderately to significantly indurated and likely has some

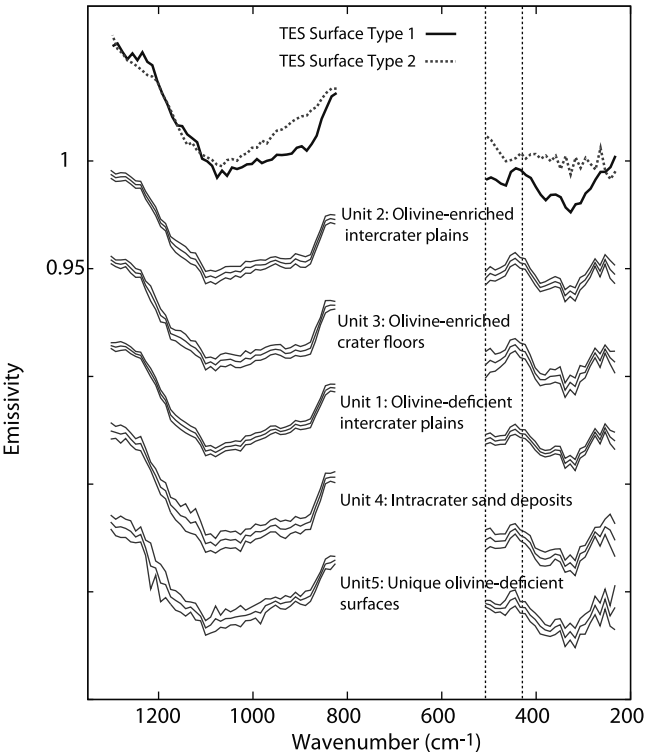

Figure 2. Average and 1σ TES surface emissivity spectra from the major units found within the study region. Table 2 gives the number of TES orbits and unit locations used in each average. Global TES-derived spectral end-members of *Bandfield et al.* [2000b] "TES surface type 1 and type 2" are shown for comparison; in general, these bracket the typical range of spectral variability on Mars. Units 2, 3, and 4 are more similar to surface type 1 than surface type 2. Units 1 and 5 are similar to surface type 1 at low wave numbers (<~507 cm^{-1}) and similar to surface type 2 at high wave numbers (>~830 cm^{-1}). Dashed vertical lines show the two spectral regions used to calculate the 507 cm^{-1} index. The units show subtle distinctions from each other in the ~430–500 cm^{-1} range and the ~875–1100 cm^{-1} range.

rocks or unconsolidated material on the surface. In defining this typical thermal inertia range for this unit, crater rims, ejecta, and interiors were intentionally avoided to obtain information about the intercrater surfaces only. Crater rims and areas near impact craters that likely contain ejecta (based on proximity to the crater rim) commonly exhibit thermal inertia values outside this range (as high as 460 $J\,m^{-2}\,K^{-1}\,s^{-1/2}$ in one instance). Conversely, instances of unit 1 found in interiors of craters commonly exhibit thermal inertia values below this range.

3.2. Unit 2: Olivine-Enriched Intercrater Plains

[17] Intercrater plains in the study region contain isolated exposures of nighttime-warm units (Figure 1) that appear more resistant than surrounding units (Figure 5). In some areas, these units embay higher-standing features (Figure 6). The resistant units are compositionally distinct from unit 1 in that they are enriched in olivine by ~5% (Table 2 and Figure 4). CRISM multispectral survey data corroborate the enrichment in olivine for most occurrences of this unit. Many occurrences also show higher TES-derived abundances of pyroxene (Figure 4).

[18] In THEMIS multispectral data, unit 2 is primarily distinguished from unit 1 by a strong absorption in band 7 (~11 μm) relative to bands 5 (~9.4 μm) and 8 (~11.8 μm), consistent with the olivine enrichment described above (Figure 3). Using bands 8-7-5 as red-green-blue in the DCS images, unit 1 typically appears greenish due to the higher ~11 μm emissivity relative to unit 2. Conversely, the relatively low ~11 μm emissivity in unit 2 causes an absence of green in the decorrelation stretch, which results in a magenta color for this unit. The strength of the ~11 μm absorption varies slightly across the region, however. In areas where

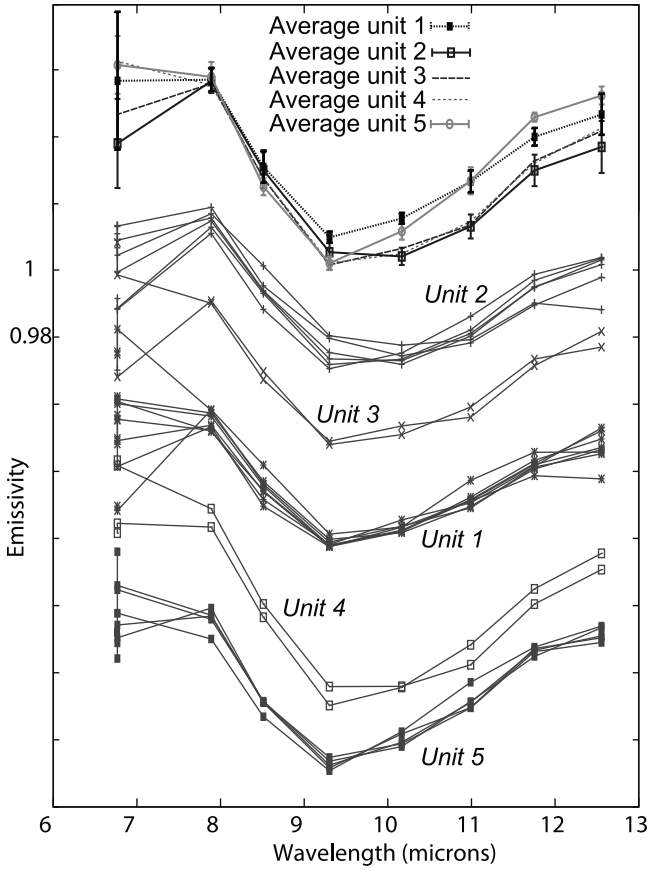

Figure 3. THEMIS surface emissivity spectra from the major units found within the study region. Spectra with italicized label font indicate that each spectrum represents the average surface emissivity from a different unit location within the study region. Some of the variability within each set of spectra may be due to real surface variability; some may also be due to slight overcorrection/undercorrection for atmospheric components between individual THEMIS images. Spectra with regular label font indicate average spectrum from each set of spectra with italicized label font, normalized to the average spectral contrast for all spectra. Standard deviations are shown for the units where five or more spectra were used to calculate the average. The average spectra from units 3 and 4 are not spectrally distinct from the average unit 2 within the wavelength range covered by THEMIS.

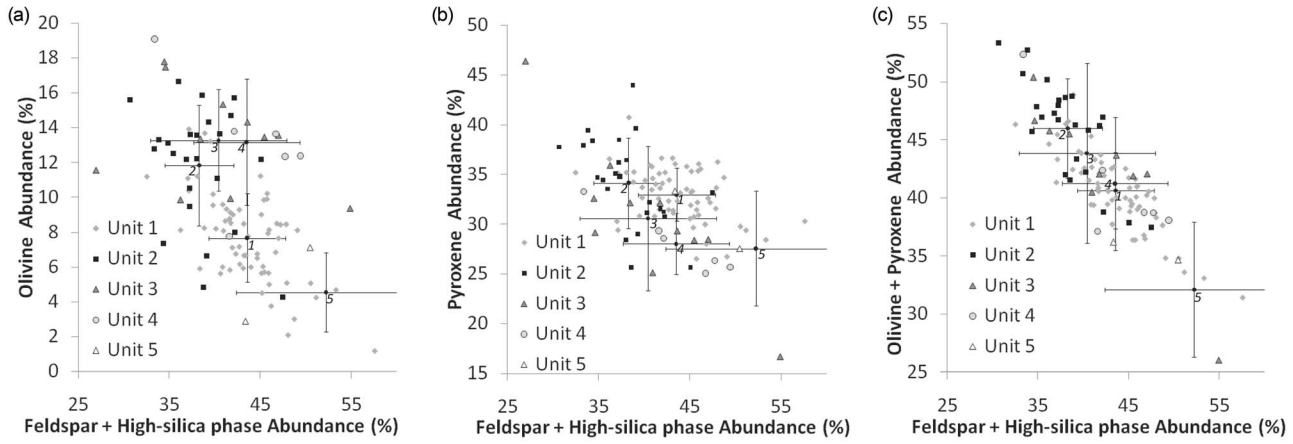

Figure 4. Scatterplots of feldspar + high-silica phase abundance versus (a) olivine, (b) pyroxene, and (c) olivine + pyroxene, for individual occurrences of each unit. The average values for occurrences of each unit are designated using the number of each unit (example: "1" = "unit 1"). The error bars represent one standard deviation around the mean. Note that these average and error values differ slightly from those in Table 2 because the unit averages in Table 2 represent mineral abundances calculated from the average surface emissivity spectrum derived for each unit (Figure 2) rather than the average mineral abundances derived from multiple locations within each unit. Using both averaging methods helps to highlight and corroborate the major compositional differences between units.

Table 2. Geologic, Thermophysical and Compositional Characteristics of Major Spectral Units in Study Region[a]

	Modeled Mineral Abundances[b]				
	Unit 1 Olivine-Deficient Intercrater Plains	Unit 2 Olivine-Enriched Intercrater Plains	Unit 3 Olivine-Enriched Intracrater Deposits	Unit 4 Intracrater Low-Albedo Sand Deposits	Unit 5 Unique Olivine-Deficient Surfaces
Feldspar	27 (4)	22 (4)	26 (4)	27 (5)	32 (4)
Pyroxene	33 (3)	34 (4)	32 (4)	28 (4)	29 (3)
Olivine	7 (2)	12 (2)	13 (3)	13 (3)	6 (3)
High-silica phases	17 (5)	18(6)	14 (6)	16 (7)	19 (5)
Other[c]	5	15	15	15	15
Number of TES orbits used in spectral average	268	56	22	13	9
Number of separate locations used in spectral average	65	24	11	6	3
Spectral properties	Low TES 507 cm^{-1} index	High TES 507 cm^{-1} index; similar to unit 3	High TES 507 cm^{-1} index; similar to unit 2	Intermediate TES 507 cm^{-1} index	Low TES 507 cm^{-1} index; low to intermediate TES 465 cm^{-1} index; higher emissivity between 10.2 and 11.8 μm in THEMIS spectra
Typical color(s) in THEMIS DCS (8-7-5 band combination)	Green, pink	Magenta	Magenta, green	Orange, pink	Yellow
Thermal inertia (J m^{-2} K^{-1} $s^{-0.5}$)	200–380	240–410	240–620	165–195	220–365
Other characteristics	Degraded and/or dissected morphlogy; includes highstanding features such as crater rims and massifs	Resistant morphology; sometimes partially covered/altered with less mafic material	Resistant morphology; sometimes partially covered/altered with less mafic material; edges of crater floors commonly more mafic	Dune forms are present in some cases	Smooth appearance in THEMIS IR in some cases; found associated with a variety of morphologic features

[a]Spectral/compositional properties not given for small-scale units.
[b]Statistical uncertainties on derived abundance are shown in parentheses.
[c]Phases modeled below detection limits for all 5 units (sulfate, carbonate, hematite, quartz).

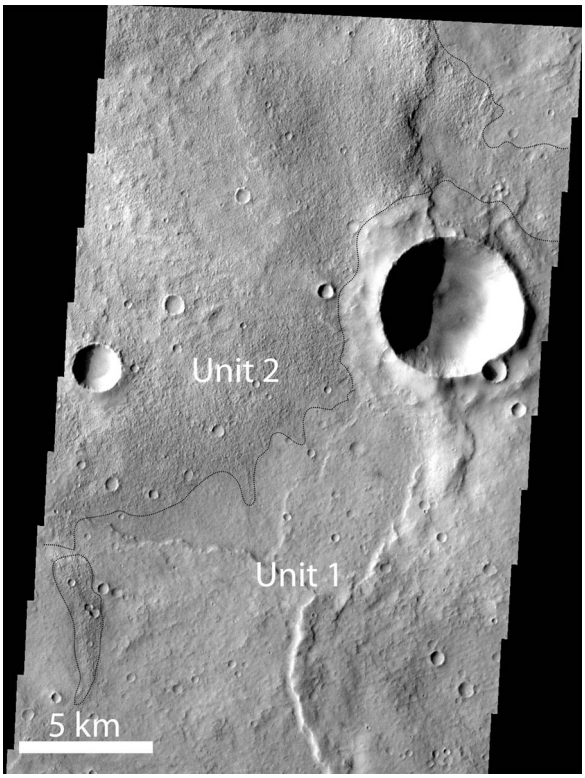

Figure 5. Portion of THEMIS VIS image V27244006 of olivine-enriched (unit 2) and olivine-deficient intercrater plains surfaces (unit 1). Location is shown in Figure 1. Note transition from resistant to degraded morphology that corresponds with the spectral boundary in Figure 1.

the ~11 μm absorption is slightly weaker, unit 2 appears more red; in areas where the ~11 μm absorption is slightly stronger than average, unit 2 appears more blue. Within the wavelength range covered by THEMIS, units 1 and 2 are spectrally similar to the two major globally derived spectral units defined with TES data by *Bandfield et al.* [2000b], referred to as "surface type 1" (similar to unit 2) and "surface type 2" (similar to unit 1) (Figure 3).

[19] As described above, in THEMIS DCS 8-7-5 images, unit 2 surfaces are usually magenta, reddish magenta or bluish magenta. However, these units are commonly partially covered in some areas by slightly less mafic materials which appear greenish yellow in THEMIS DCS 8-7-5 images (area C in Figure 1). The deposits are inferred to be slightly less mafic on the basis of slightly higher emissivity at ~11–11.8 μm (Figure 7) [e.g., *Lyon*, 1965], similarity to unit 1, and lower olivine parameter strength in CRISM data. Because of the spectral similarity to unit 1, these overlying deposits are not classified as a distinct spectral unit. These deposits drape underlying topography (Figure 8) and excavated material from craters which impacted into these surfaces are spectrally similar to unit 2; both observations suggest that the overlying deposits are not of substantial thickness. Nighttime radiance values do not necessarily correspond with the presence/absence of this material; in some cases, it is decreased whereas in others it is unchanged. This suggests that the deposits are of variable thickness. The spectral differences between unit 2 and overlying deposits are not distinguishable in TES data in all occurrences; however, in some cases, slight differences are observed. The disconnect between TES and THEMIS data is likely related to the differences in spatial resolution. With THEMIS, hundreds of spectra can be isolated from these deposits to increase the signal-to-noise ratio; with TES, only a few spectra that cover these deposits can be averaged and thus sometimes the deposits are not statistically distinguishable from the surrounding unit 2.

[20] Relative to olivine-deficient, less resistant intercrater plains (unit 1), the unit 2 occurrences exhibit a strong negative emissivity slope between ~430 and ~508 cm^{-1} (Figure 9a). This is the most consistently distinct spectral region for these two units, where the emissivity slope in this range is controlled by relative olivine and/or pyroxene abundance relative to plagioclase and/or high-silica phase abundance (Figure 9b). This spectral region is not significantly affected by atmospheric dust loading or changes in atmospheric path length, and thus a spectral index that maps the magnitude of that slope may be applied to emissivity data with or without an atmospheric correction. An example TES 507 cm^{-1} index map is shown in Figure 10. Strong 507 cm^{-1} index values have a high spatial correspondence with resistant, daytime-cool/nighttime-warm intercrater plains units that appear magenta in THEMIS DCS 8-7-5 images. The TES 507 cm^{-1} index, along with THEMIS DCS 8-7-5 images, was used to locate all occurrences of olivine-enriched intercrater plains (unit 2) (Figure 11).

[21] Typically, the thermal inertia of unit 2 appears mottled (Figure 1), and ranges from ~240 to ~410 J m^{-2} K^{-1} $s^{-1/2}$. In general, the lower thermal inertia areas are associated with the portions of unit 2 that have the overlying less mafic deposits (described above). Conversely, areas that are free of these overlying deposits have distinctly higher nighttime

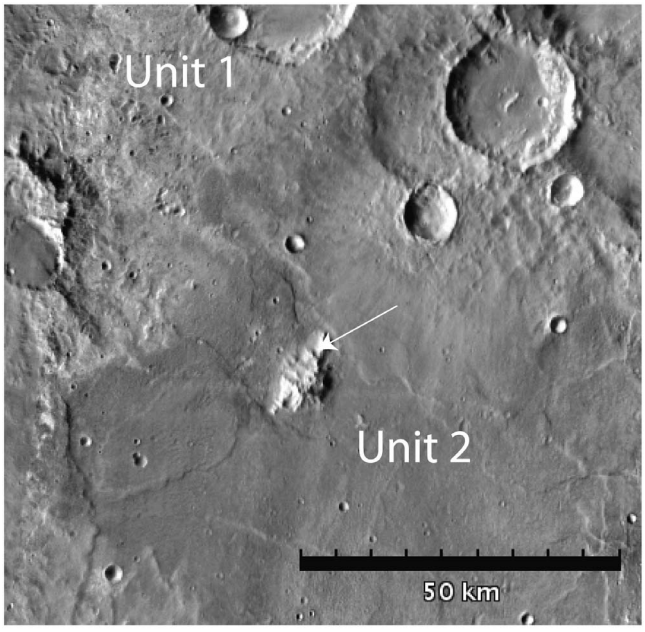

Figure 6. THEMIS daytime radiance mosaic centered at 77.8°E, 6.8°S. Example of embayment relationship between unit 2 and older, highstanding degraded plains materials (unit 1, arrow).

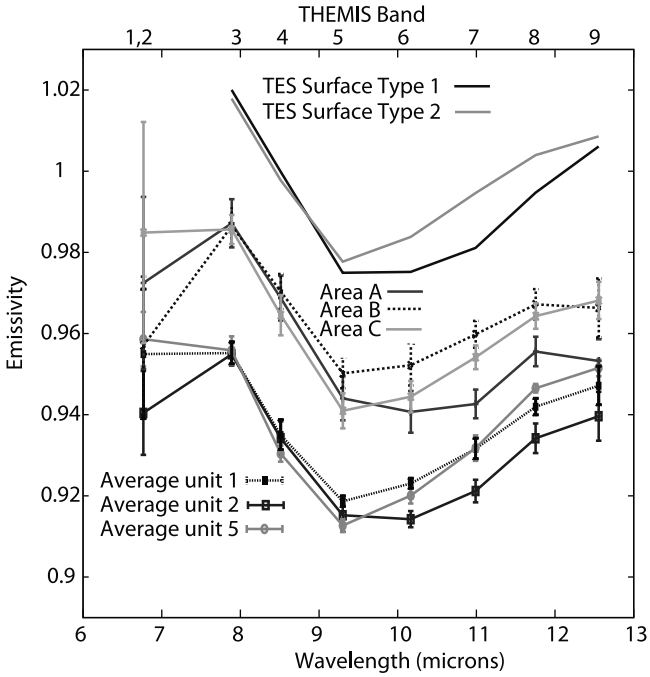

Figure 7. THEMIS surface spectra from areas shown in Figure 1. Note that area C is spectrally similar to area B but has thermophysical properties that are similar to area A. Spectra are compared with the average unit spectra from Figure 3 and with TES surface types 1 and 2 [*Bandfield et al.*, 2000b].

radiance values than the surrounding area (Figure 1). The thermophysical boundaries of this unit commonly coincide with the compositional boundaries. Rare instances where thermal inertia boundaries do not obviously correspond with areas highlighted by the 507 cm^{-1} index may be related to local derivation of sediment (meaning, from rocks directly underlying the sediment surface), which would lower the thermal inertia within unit 2.

3.3. Unit 3: Olivine-Enriched Intracrater Deposits

[22] Numerous craters in the region have shallow, relatively flat floors (gradient <1%) that commonly exhibit high TES 507 cm^{-1} index values and are compositionally indistinguishable from the olivine-enriched intercrater plains (unit 2) (Table 2 and Figure 4). Figure 11 shows the distribution of crater floors with high TES 507 cm^{-1} index values in addition to intercrater plains surfaces with high index values. This unit typically appears magenta in DCS 8-7-5 images.

[23] Unit 3 is always thermophysically distinct from the surrounding plains surface and is typically some of the highest thermal inertia material in the area. The thermal inertia typically ranges from ~240 to ~425 J m^{-2} K^{-1} $s^{-1/2}$, but there are some instances where the thermal inertia is as high as 620 J m^{-2} K^{-1} $s^{-1/2}$. This broad thermal inertia range likely indicates unconsolidated material present within the crater that causes such variation in the thermal inertia. This interpretation is confirmed by the presence of low albedo surfaces with diffuse boundaries observed in CTX images, suggesting the presence of a thin layer of unconsolidated sand in portions of this unit. Some craters have thermophysically distinct materials on their floors but do not exhibit a strong 507 cm^{-1} index value. These craters may have been resurfaced by sediment derived from unit 1, or may have been similar to other unit 3 occurrences but chemically/mechanically altered to change the spectral signature. The thermal inertia signature could be preserved if alteration or resurfacing affected only a thin surface layer, because spectral measurements are sensitive to the upper few hundred microns or less and thermal inertia is sensitive to the upper few centimeters of material. In other cases, the 507 cm^{-1} index maps a wider area of material than is thermophysically distinct from the surrounding surface; this difference may be due to material that has mechanically eroded from the floor or walls of the crater yet has the same composition (example, Figure 7).

[24] The surface morphometry of these units and their margins were examined for all occurrences where topographic information was publicly available from HRSC. Though the unit 3 occurrences are relatively flat, in many cases the margin appears to rise upwards and conform to the lower portion of the crater wall (Figure 7). In fewer examples,

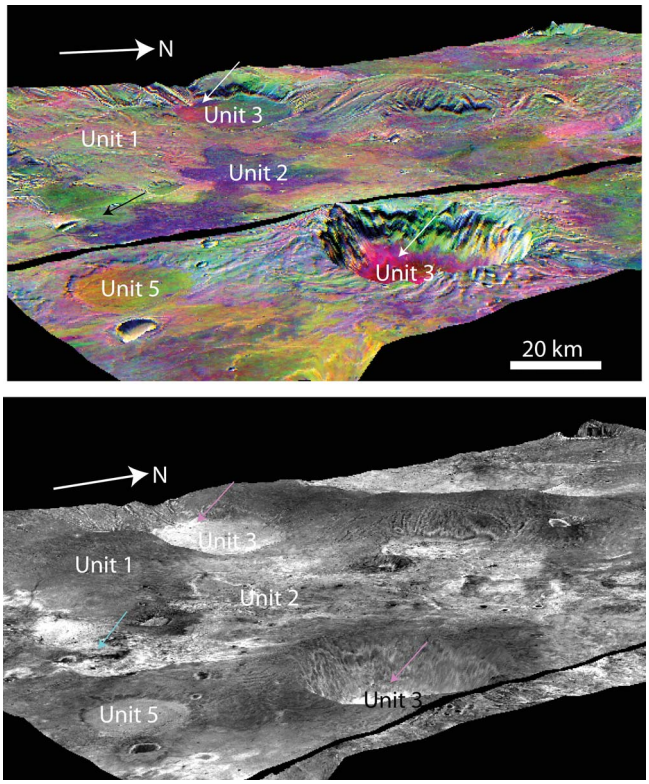

Figure 8. Portion of (top) THEMIS DCS mosaic and (bottom) THEMIS nighttime radiance mosaic from Figure 1, draped over HRSC DTM (image ID: h0532_0000_DT4). View is looking toward the northwest. Vertical exaggeration is 4X. In Figure 8 (top), white arrows point to margins of unit 3, which conform to the edges of the crater walls (arrows are pink in Figure 8 (bottom)). Note that the unit margin is lower thermal inertia (lower nighttime radiance) than the interior of the unit (see sections 3.3 and 4.1.3 for details). Black arrow (cyan in Figure 8 (bottom)) points to less mafic deposits which overlie unit 2.

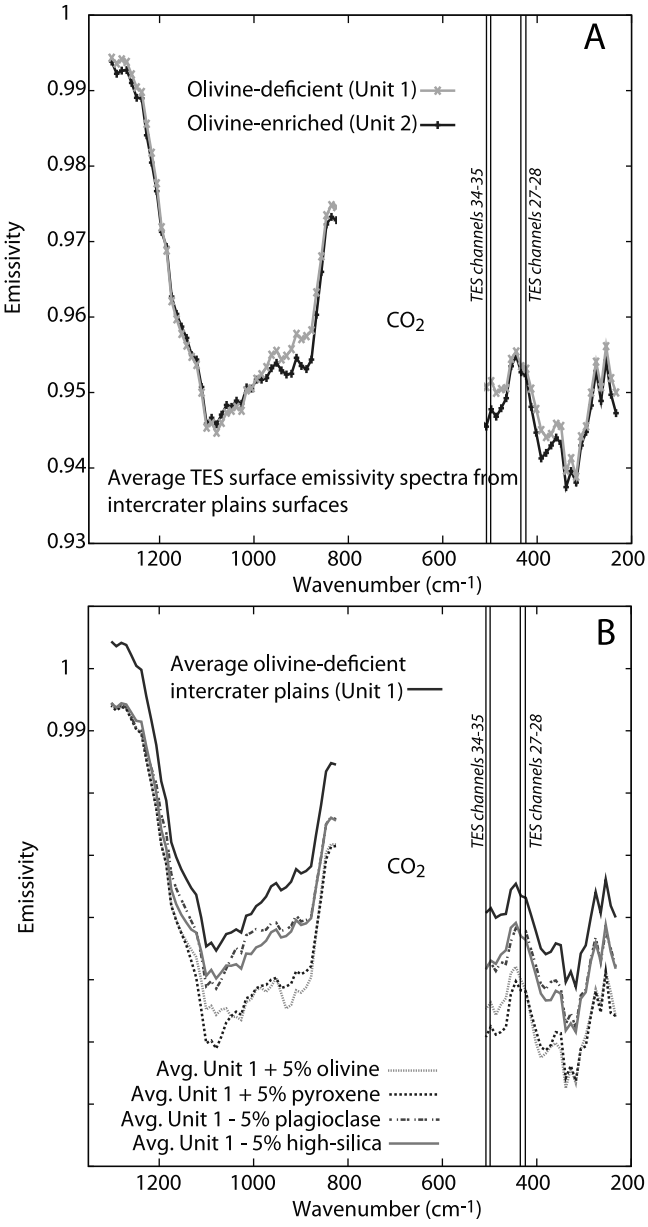

Figure 9. (a) Average TES emissivity spectra of olivine-enriched and olivine-deficient intercrater plains from Figure 2. These units are primarily distinguished in the ~900 cm^{-1} and 450 cm^{-1} regions. The ratio of average emissivity in TES channels 27–28 and 34–35 was used to develop the "507 cm^{-1} index." High values of the index indicate a sharp decrease in emissivity between ~430 and ~500 cm^{-1}, which is characteristic of the olivine-enriched intercrater plains. (b) Effect of addition of olivine/pyroxene or subtraction of plagioclase/high-silica phases from typical intercrater plains materials (e.g., unit 1). The 507 cm^{-1} index value (ratio of TES channels 27–28 to 34–35) is increased with (1) increased olivine and/or pyroxene or (2) decreased plagioclase and/or high-silica phases. Solid black spectrum is offset by +0.01 emissivity for clarity.

the margin of unit 3 stops short of the crater wall, and forms one side of a trough with slump material from the crater wall (Figure 12). A random survey of ~10 craters shows that unit 3 surfaces (the crater floors) are shallow relative to the crater diameter. For the examples studied, crater floor depths ranged from ~500 to 1200 m for crater diameters of ~35 to 75 km, resulting in depth/diameter ratios <0.027. Using the depth/diameter relationships for relatively fresh Martian complex craters (>8 km) established by *Garvin et al.* [2000] and *D. E. Smith et al.* [2001], these craters likely had depths ranging between ~2 and 3 km and depth/diameter ratios between 0.038 and 0.052 at the time of completion of the crater modification stage (stages described by *French* [1998]). The measured present-day crater floor depths imply that an extra ~1–2 km of material overlies the fallback breccias and impact melts which formed the original floor of these craters.

[25] As described for unit 2, many exposures of unit 3 contain overlying deposits that can exhibit a lower thermal inertia and that are spectrally similar to the olivine-deficient intercrater plains (unit 1) (Figures 13 and 14). These deposits tend to be concentrated at the center of the crater floor, resulting in a "ring" pattern (Figure 14). In many cases, the rings represent the slightly steeper or raised edges of the crater floor where rockier, olivine-enriched material is exposed (white arrow in Figure 12).

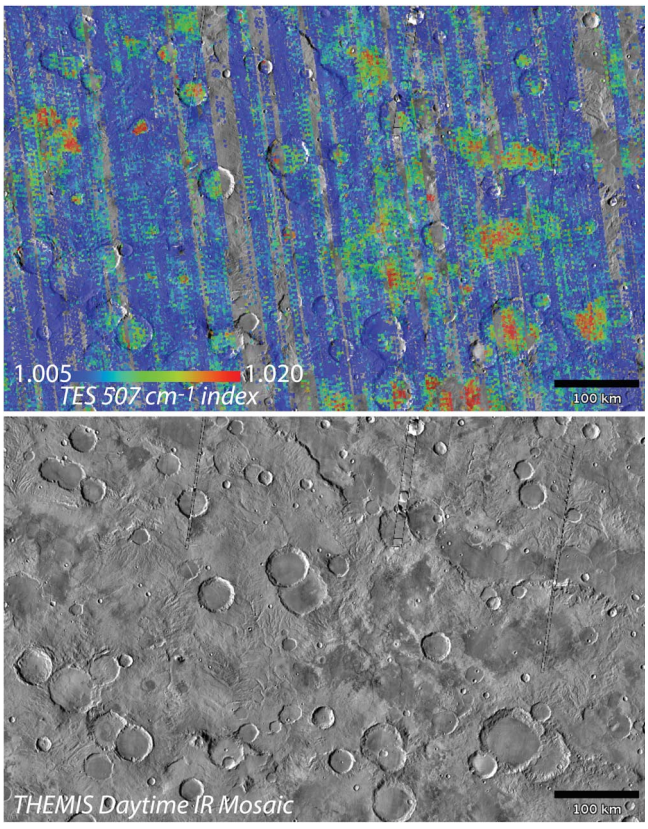

Figure 10. A TES 507 cm^{-1} index map centered at 72.2°E, 11.4°S. High values of the index have a close spatial correspondence with daytime-cool intercrater plains surfaces (unit 2) and consolidated intracrater deposits (unit 3) in the study region.

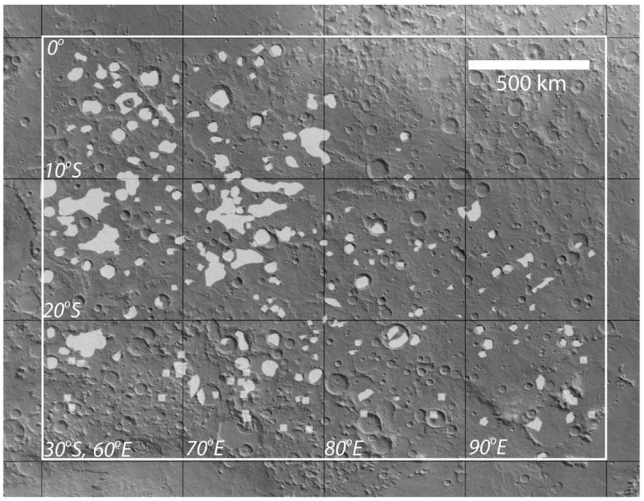

Figure 11. Locations of olivine-enriched intercrater plains (unit 2) and crater floors (unit 3) based on the TES 507 cm^{-1} index. Volcanic plains from Syrtis and Hesperia Planums are excluded from the mapping effort. The base image is TES albedo overlying MOLA shaded relief. The northeast corner of the study region is affected by surface dust (brighter area).

3.4. Unit 4: Intracrater Sand Deposits

[26] Intracrater sand deposits were identified using THEMIS DCS and visible images. Sand deposits typically appear as bright pink or orange in DCS 8-7-5 combinations, are dark toned, and commonly contain dune forms or ripple morphologies (Figure 15). These deposits are relatively free of dust, as indicated by high 1350–1400 cm^{-1} emissivity values (>0.98) [*Ruff and Christensen*, 2002] and low albedo (<0.11). TES spectra of these sand deposits indicate that, compositionally, they are similar to olivine-enriched intercrater plains and crater floors (units 2 and 3) (Table 2 and Figure 4), with perhaps a slightly higher abundance of feldspar and/or high-silica phases (Figure 4). Spectrally, the 507 cm^{-1} feature is not as strong (Figure 2), suggesting that this unit is intermediate between unit 1 and units 2–3. Intracrater sand compositions do not vary significantly within the study region.

[27] Many of the sand deposits are sufficiently small that THEMIS thermal inertia pixels include mixtures of sand and the surrounding, often higher thermal inertia, crater floor material. However, some sand deposits are larger and form dunes. These dunes have the lowest thermal inertia in the unit, and the thermal inertia of these materials are likely representative of the sand alone and have the least amount of subpixel mixing. It is these examples that we have used to define the thermal inertia of this unit. The thermal inertia ranges from ~165 J m^{-2} K^{-1} $s^{-1/2}$ to ~195 J m^{-2} K^{-1} $s^{-1/2}$, which corresponds to fine sand, and is within the range of thermal inertia values derived at the MER-A and MER-B landing sites for intracrater bed forms [*Fergason et al.*, 2006b] and bed forms observed from orbit [e.g., *Edgett and Christensen*, 1991, 1994; *Fenton et al.*, 2003].

3.5. Unit 5: Unique Olivine-Deficient Surfaces

[28] Some surfaces appear bright yellow in THEMIS DCS 8-7-5 mosaics (Figures 1 and 16) and commonly have a relatively smooth, featureless appearance in THEMIS IR images. Higher resolution images from CTX, available for two occurrences, show a smooth, featureless surface (Figure 17). Occurrences of unit 5 are shown in Figure 18. A similar spectral unit was also observed within an alluvial fan com-

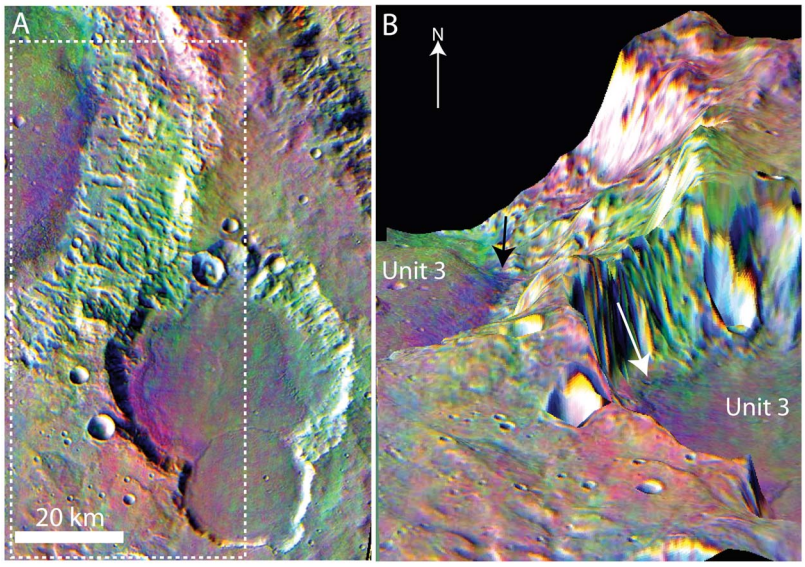

Figure 12. (a) THEMIS DCS mosaic centered near 67.7°E, 3.5°S showing two exposures of unit 3 material. White dashed line shows location of Figure 12b. (b) THEMIS DCS mosaic draped over HRSC DTM (image ID: h1968_0000_DT4). View is looking toward the north. Vertical exaggeration is 5×. White arrow points to strong unit 3 signature which corresponds with a topographic "bench" around the margin of the unit. Black arrow points to trough which is bounded on one side by unit 3 and on the other side by debris/talus from the crater wall.

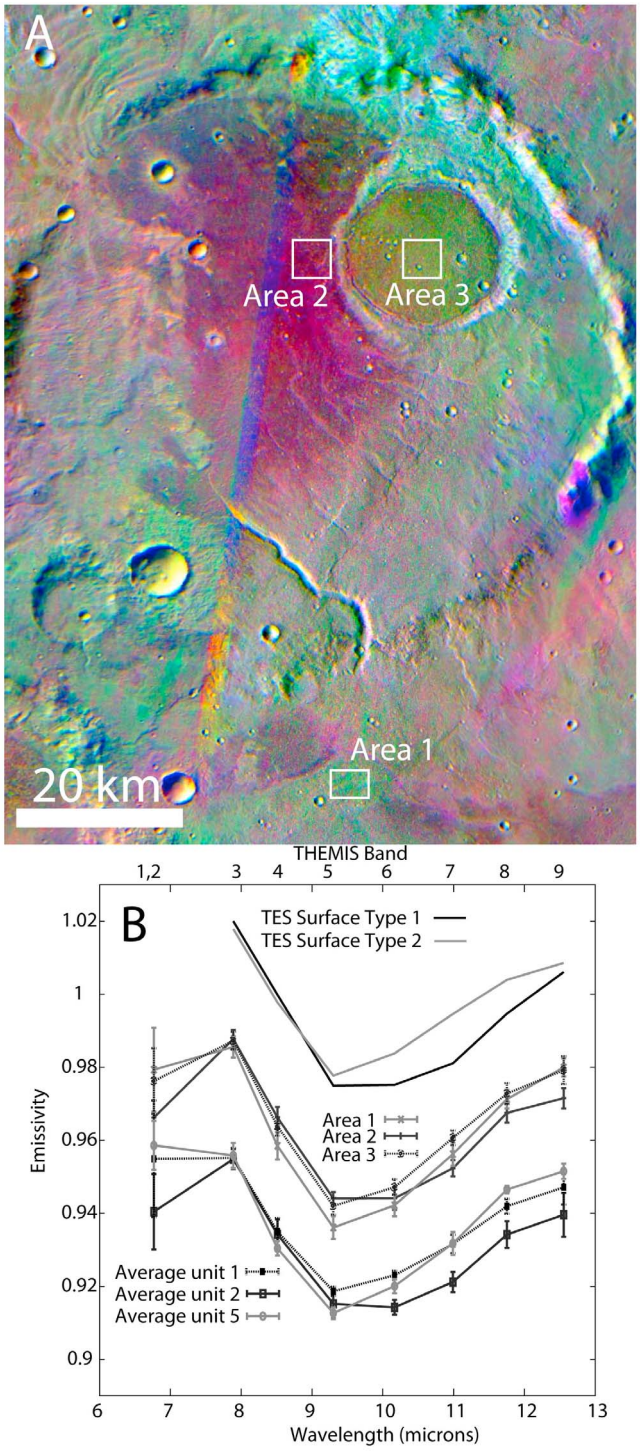

Figure 13. (a) THEMIS DCS 8-7-5 radiance mosaic showing olivine-enriched crater floor (unit 3) that contains a smaller crater with different spectral properties in THEMIS. The smaller crater floor surface is ~15 m higher in elevation than the larger crater floor surface. (b) THEMIS spectra from areas shown in Figure 13a compared with average unit spectra from Figure 3 and with TES surface types 1 and 2 [*Bandfield et al.*, 2000b]. The smaller crater surface (area 3) is more similar to area 1 (unit 1) than area 2 (unit 2).

plex in the study region by *Williams et al.* [2011]. A HiRISE scene over the alluvial fan spectral unit shows a rugged, pitted texture [*Williams et al.*, 2011, Figure 2].

[29] Unit 5 appears to be associated with a variety of geomorphic surface types. Aside from the alluvial fan complex, unit 5 is found associated with isolated buttes/massifs (Figures 16 and 19), on talus materials eroded from unit 1 (example, Figure 19), as well as in smooth surfaces overlying units 1, 2, or 3. The boundaries of these units are

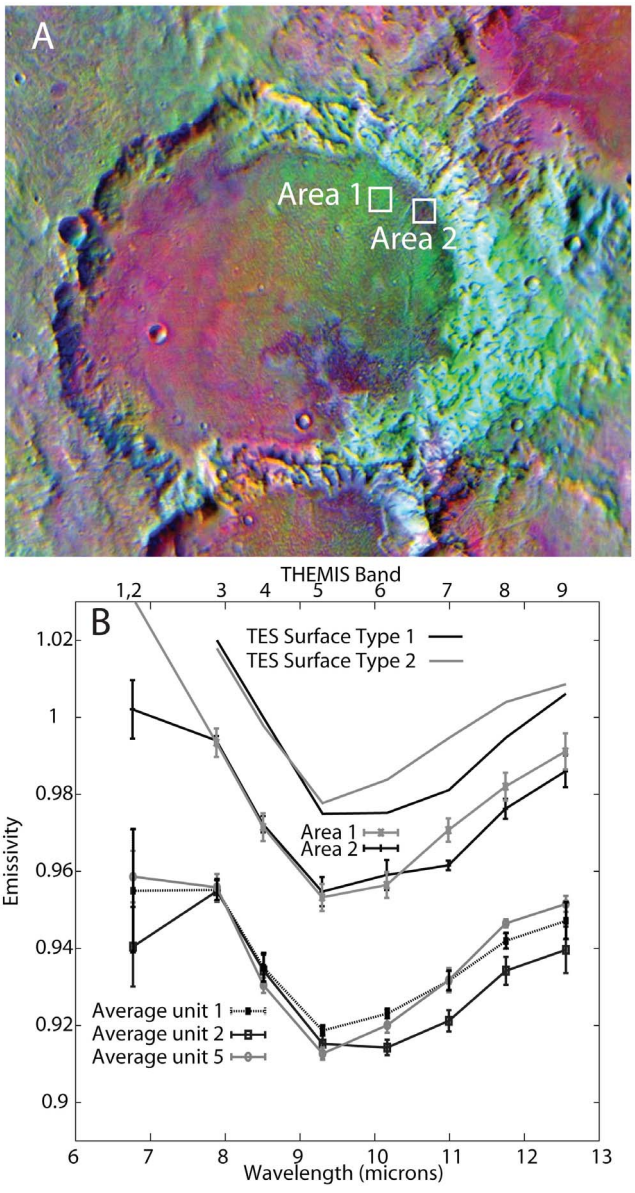

Figure 14. Example (centered at 66.1°E, 3.1°S) of flat-floored crater with "ring" pattern of lower thermal inertia, less mafic material surrounded by higher thermal inertia, olivine-enriched material. (a) THEMIS DCS 8-7-5 radiance mosaic. (b) THEMIS surface emissivity spectra from areas shown in Figure 14a, compared with the average unit spectra from Figure 3 and with TES surface types 1 and 2 [*Bandfield et al.*, 2000b]. Area 1 is spectrally similar to unit 1, whereas area 2 is spectrally similar to unit 2.

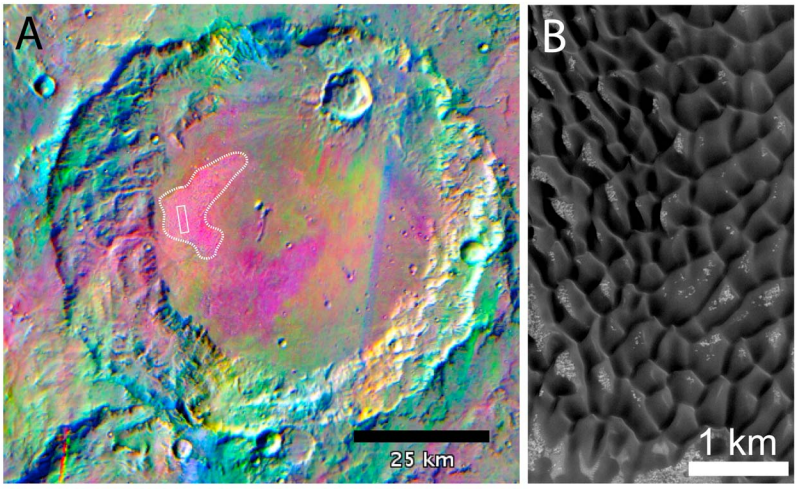

Figure 15. Example intracrater sand deposit, centered at 98.0°E, 14.6°S. (a) THEMIS DCS mosaic, bands 8-7-5 as R-G-B. (b) Portion of MOC NA image within deposit.

relatively distinct, suggesting that they are true geomorphic units rather than sediment easily transported by saltation.

[30] The unit 5 spectral average is compositionally indistinguishable from olivine-deficient intercrater plains (unit 1) (Table 2), but there is high variability in the derived mineral abundances from individual occurrences. In general, the unit is deficient in olivine and pyroxene relative to units 2–3 but within the range of olivine and pyroxene abundance of unit 1. Feldspar and/or high-silica phase abundances may be slightly higher in unit 5 as well (Figure 4). The unit clearly has a distinct spectral signature in THEMIS, with higher emissivity in bands 6–8 (Figure 3). With one excep-

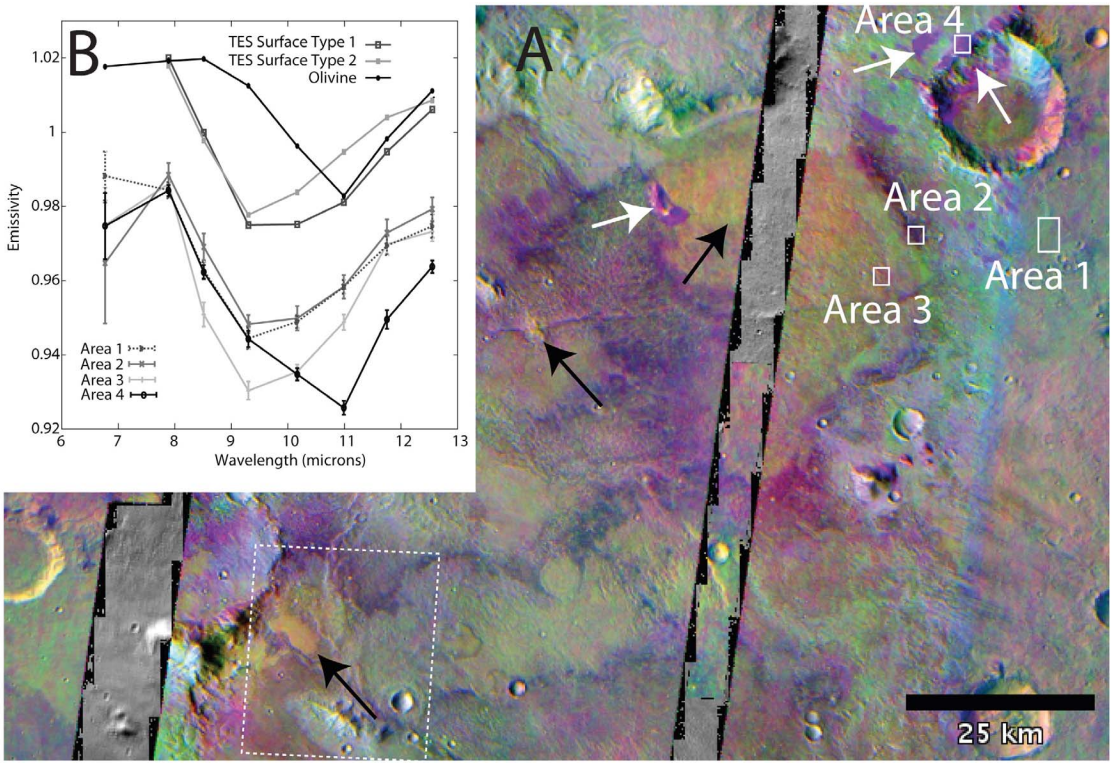

Figure 16. Examples of olivine-rich outcrops, olivine-enriched (unit 2) and olivine-deficient (unit 1) intercrater plains, and unique olivine-deficient surfaces (unit 5) in THEMIS DCS radiance mosaics, using bands 8-7-5 displayed as R-G-B. (a) Mosaic centered at 63.0°E, 21.6°S. White arrows point to olivine-rich outcrops; black arrows point to unique olivine-deficient surfaces (unit 5). Dashed box outlines location of Figure 17b. (b) THEMIS surface spectra from areas indicated in Figure 16a compared with TES surface types 1 and 2 [*Bandfield et al.*, 2000b] and an olivine spectrum.

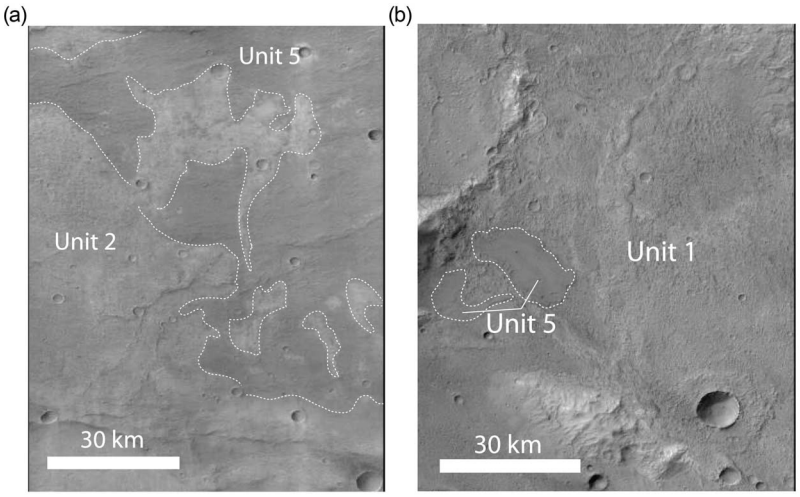

Figure 17. (a) Portion of CTX image P11_005460_1667_XI_13S294W, centered at 65.4°E, 14.8°S, showing textural appearance of unit 5. (b) Portion of CTX image B17_016246_1593_XN_20S297W, centered at 62.5°E, 22.2°S, showing textural appearance of unit 5. Image location is shown in Figure 16.

tion, these surfaces do not exhibit high (>1.01) 465 cm^{-1} index values and are generally not spectrally distinguished from unit 1 in TES data (Figure 2). As described in section 3.1, the disconnect between TES and THEMIS spectral distinctions is likely related to the differences in signal-to-noise ratio achieved with THEMIS spectral averages compared to TES spectral averages. The THEMIS signature of unit 5 is consistent with either a slight enrichment of high-silica phases or simply a more felsic lithology [e.g., *Lyon*, 1965] (meaning higher plagioclase/(pyroxene+olivine) ratio) relative to units 1 and 2. There are no apparent pyroxene, olivine or hydration signatures associated with this unit in CRISM multispectral survey data.

[31] The thermal inertia of this unit ranges from ~220 to ~365 J m^{-2} K^{-1} $s^{-1/2}$. It is typically thermophysically distinct from the surrounding region, but only by a slight amount (~40 J m^{-2} K^{-1} $s^{-1/2}$ higher than surroundings). As with its geomorphic associations, the thermal inertia characteristics are not consistent between exposures. In some cases the unit is thermophysically uniform, whereas in others, patches of higher thermal inertia materials are mixed within this unit at 100 m scales.

3.6. Rare or Small-Scale Units

[32] Several units were observed in THEMIS DCS 8-7-5 mosaics or in TES 507 cm^{-1} index maps that are either isolated occurrences, too small to be resolved in TES data, or already described elsewhere. These include: olivine-rich outcrops and crater central uplifts, a pyroxene-enriched isolated massif, and likely chloride deposits [*Osterloo et al.*, 2008]. Olivine-rich outcrops have a stronger spectral absorption at ~11.0 μm relative to olivine-enriched intercrater plains and crater floors (units 2 and 3) and typically appear bright purple in THEMIS DCS 8-7-5 mosaics (Figure 16). These outcrops are identified as olivine-rich on the basis of THEMIS and CRISM spectral properties; additionally, some of the larger outcrops can be identified in 16 pixel-per-degree TES olivine index maps [*Koeppen and Hamilton*, 2008]. A few crater central uplifts were observed to exhibit a color difference from the olivine-deficient intercrater plains (unit 1) in THEMIS DCS images (example, Figure 20). In the example shown, TES, THEMIS, and CRISM data all confirm that the central uplift and parts of the crater wall are enriched in olivine.

[33] An isolated massif in the southeastern corner of the study region was observed to have very strong TES 507 cm^{-1} index values but did not appear magenta in THEMIS DCS 8-7-5 images, unlike the olivine-enriched intercrater plains (unit 2). The TES surface emissivity spectra show a unique shape that is consistent with >50% low-Ca pyroxene (Figure 21). The low-Ca pyroxene identification is corroborated in CRISM multispectral survey data.

[34] Hundreds of likely chloride-bearing units have been identified in the Martian highlands using THEMIS DCS images; the spectral properties and chloride interpretation of these units are described in detail by *Osterloo et al.* [2008, 2010]. Several likely chloride deposits are found within the

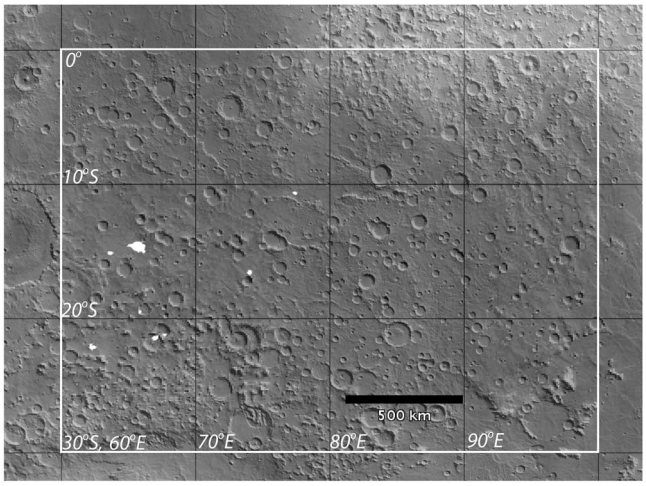

Figure 18. Locations of unique olivine-deficient units (unit 5).

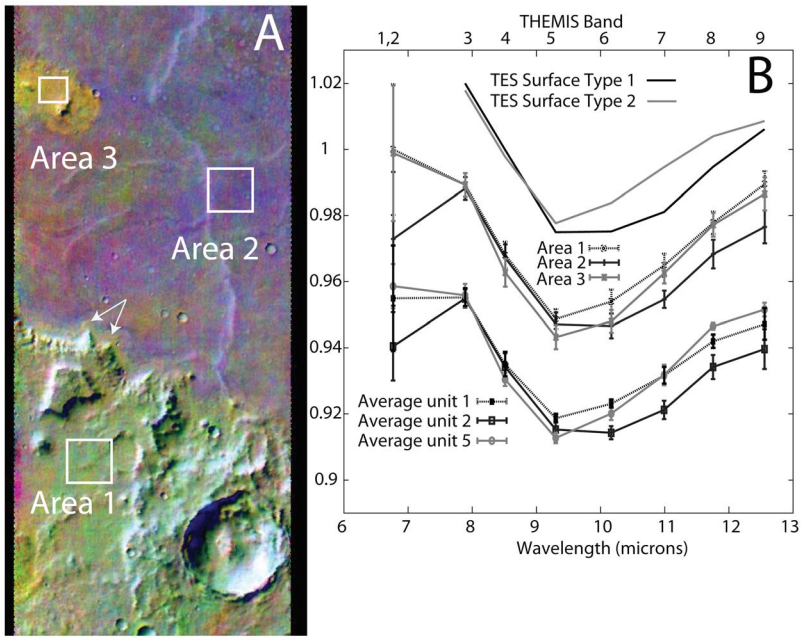

Figure 19. Examples of unit 5 associated with an isolated massif (area 3) that is embayed by unit 2 (area 2), and with talus material (arrows) eroded from a scarp within unit 1 (area 1). (a) THEMIS DCS 8-7-5 image centered at 77.5°E, 11.0°S. (b) THEMIS surface emissivity spectra from areas shown in Figure 19a, compared with average THEMIS surface emissivity spectra from Figure 3 and with TES surface types 1 and 2 [*Bandfield et al.*, 2000b].

study region [*Osterloo et al.*, 2010], all overlying areas mapped as unit 1. A few of the chloride deposits were selected for retrieval of thermal inertia; these occurrences all exhibit a higher thermal inertia than the immediately surrounding terrain (90–170 J m^{-2} K^{-1} $s^{-1/2}$ difference). The thermal inertia values are consistent throughout this unit and range from ~420 to ~480 J m^{-2} K^{-1} $s^{-1/2}$, exactly within the range reported by *Osterloo et al.* [2010]. Interestingly, though the unit 1 surfaces associated with the chlorides exhibit low 507 cm^{-1} index values and relatively low thermal inertia values (typical of unit 1), the morphology does appear more similar to that of unit 2, and in most cases there is a hint of the magenta color in THEMIS DCS 8-7-5 images that is typical of unit 2 (example, Figure 22). It is possible that these areas are more heavily altered versions of unit 2, such that the TES spectral characteristics typical of unit 2 are no longer present. It is not clear if this observation is relevant to the formation mechanism of the likely chloride deposits.

3.7. Other Surfaces of Interest: Thermally Distinct Crater Ejecta

[35] Most craters in the region have been heavily degraded from burial or erosion. Commonly the ejecta blankets are not discernible in visible images, but are in some cases apparent in nighttime radiance images. Dozens of craters are observed to have thermally distinct ejecta blankets in THEMIS nighttime radiance images (Figure 23) [*Rogers*, 2011]. The preservation of the thermal contrast between the ejecta and surrounding material suggests that the ejecta have not been entirely obscured or homogenized with regionally derived sediment. Indeed, approximately 35% of these thermally distinct craters exhibit a spectral difference from target materials; the spectral difference is consistent with an increase in plagioclase or high-silica phases relative to pyroxene in the exposed ejecta, relative to target surfaces [*Rogers*, 2011]. The compositional pattern may be due to vertical crustal variations in primary lithology, subsurface alteration exposed by impact, synimpact or postimpact alteration of shocked or vitrified materials, or because the target materials have experienced light surficial alteration and the impact exposed less altered materials. Observations and interpretations of these craters are described in detail by *Rogers* [2011].

3.8. Spatial, Stratigraphic, and Compositional Relationships

[36] Olivine-enriched intercrater plains units (unit 2) and crater floor materials (unit 3) are inferred to be younger than surrounding olivine-deficient plains. This is because they appear less degraded, with a resistant morphology (Figure 5), and less heavily cratered. In some areas they appear to embay degraded crater plains materials (Figure 6), also suggesting that they were emplaced on top of the degraded plains. Craters which impact into unit 2 can have ejecta with spectral properties that are similar to the target surface; but most commonly, crater ejecta are spectrally similar to unit 1. Assuming that the craters with unit 1-like spectral properties represent excavation of unit 1 from underneath unit 2, the diameters of these craters can be used to place thickness constraints on unit 2. Some craters as small as 1 km located within unit 2 were observed to have unit 1-like spectral properties; conversely, some craters as large as 5 km located within unit 2 were observed to have unit 2-like spectral properties. The amount of stratigraphic uplift experienced by target rocks during impact can be approximated as one tenth

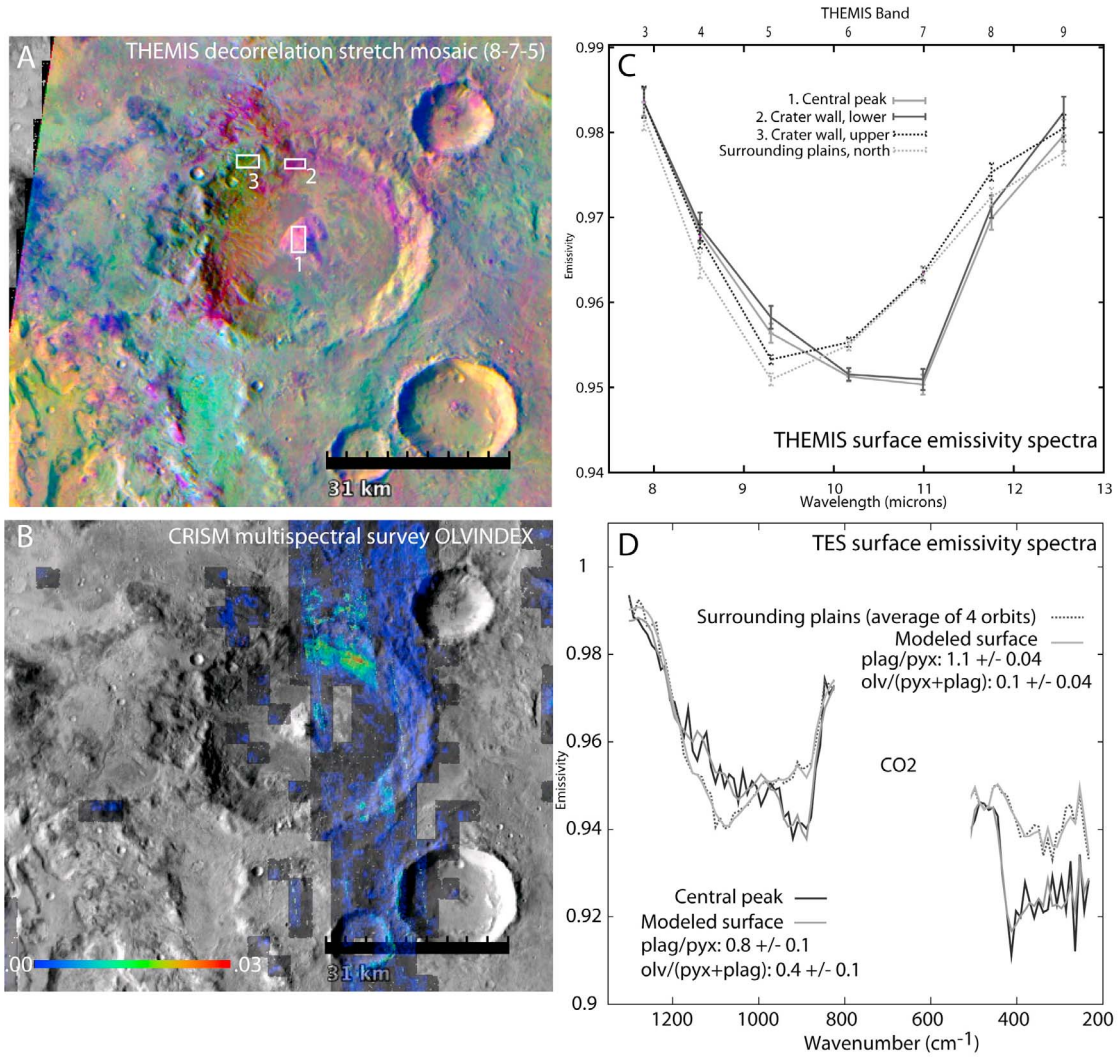

Figure 20. Example of spectrally unique crater central peak and crater wall. (a) THEMIS DCS mosaic (8-7-5 as R-G-B) centered at 75.9°E, 26.6°S. Boxes indicate locations of average spectra in Figure 20c. (b) CRISM olivine index overlain on THEMIS daytime radiance mosaic. (c) THEMIS surface emissivity spectra from the central peak, two locations on the crater wall, and olivine-deficient intercrater plains just north of image boundary. (d) TES surface emissivity spectra and derived plagioclase/pyroxene and olivine/(pyroxene + plagioclase) ratios from the central peak and the olivine-deficient intercrater plains.

the final crater diameter [*French*, 1998], which places an upper limit on the original depth of materials in the ejecta blanket. Based on the observation that craters as large as 5 km were observed to have unit 2-like spectral properties and craters as small as 1 km commonly have unit 1-like spectral properties, unit 2 is estimated to vary between <100 and <500 m thick. This estimate is consistent with thickness estimates for Noachian and Hesperian volcanic plains (~140–240 m thick), which were derived using independent means [e.g., *Greeley and Schneid*, 1991].

[37] Unit 5 is found overlying units 1, 2 and 3; however, the relative age for all occurrences of this unit is not well constrained. In many cases unit 5 is found in association with only one of the other units, thereby constraining its age only relative to the unit it overlies in that particular area. In other words, the stratigraphic position of unit 5 is not constrained on a regional scale.

[38] As described above, putative chloride deposits are found overlying unit 1 but never found in association with units 2, 3 or 5. However, as described in section 3.6, the surfaces that host the chloride units bear strong resemblance to unit 2 in morphology and THEMIS DCS images (Figure 22), despite the lack of a strong TES 507 cm^{-1} index value, and may be degraded occurrences of unit 2. The lack of chloride deposits on crater floors or on unambiguous unit 2 type surfaces is interesting; however, the rarity of their occurrence in general precludes any meaningful inference for the origin or environmental conditions required for the chloride deposits.

[39] Phyllosilicate-bearing surfaces, inferred from mapping 2.3 μm depth from CRISM multispectral summary products (the D2300 parameter; see *Rogers* [2011] for a map of D2300 detections in this region) are confined to two major subregions within the study area. In the northeast portion of the study region, elevated D2300 parameter values

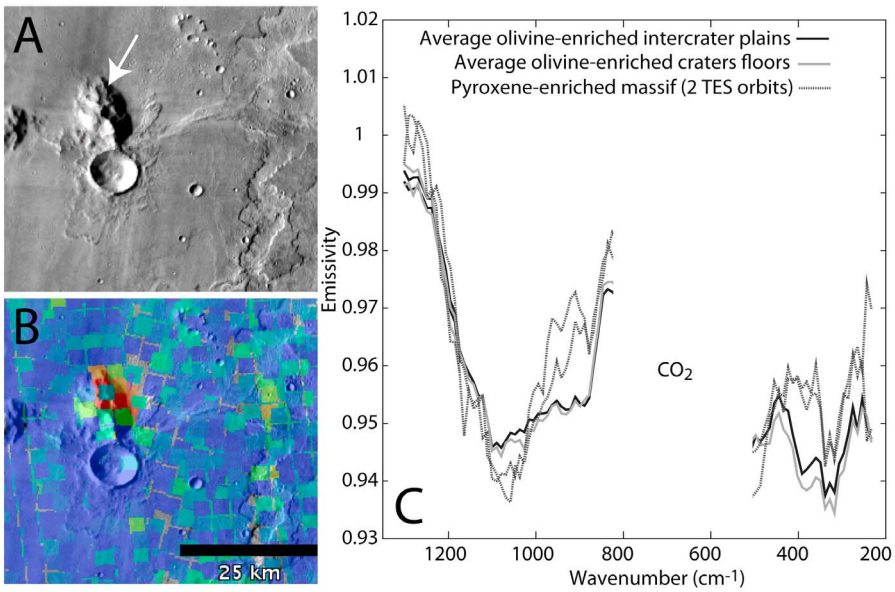

Figure 21. Unique, pyroxene enriched massif near 98.7°E, 23.0°S identified from very high TES 507 cm^{-1} index values. (a) THEMIS daytime radiance mosaic of massif. (b) TES 507 cm^{-1} index map (index scale bar is the same as in Figure 10). (c) TES surface emissivity spectra from the massif, derived from two different orbits (dashed), compared with average emissivity spectra from the olivine-enriched intercrater plains and crater floors (units 2 and 3).

are mostly found in association with crater materials (ejecta, walls, rims or central uplifts), as also reported by [*Mustard et al.*, 2008]. Some of the phyllosilicate-bearing craters are as small as 2 km in diameter. A few detections were also identified in unit 1, in a low-lying valley rimmed by dissected surfaces near 88.6°E, 5.0°S. In the southwestern part of the study region, elevated D2300 parameter values are found within unit 1 and are associated with buttes, crater

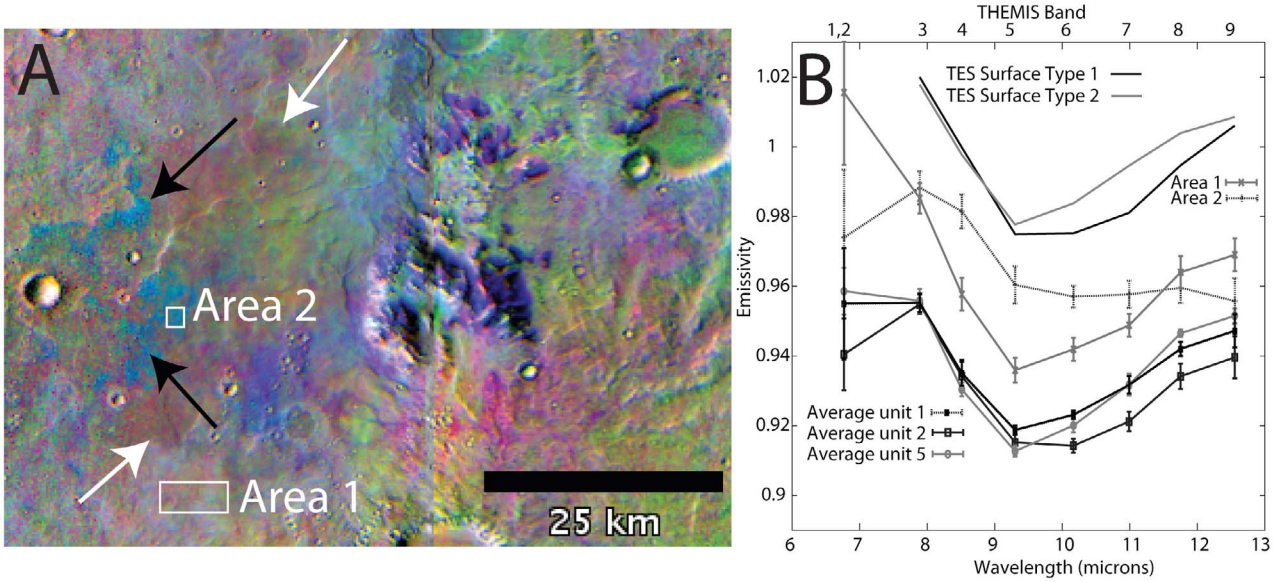

Figure 22. Examples of probable chloride deposits in THEMIS DCS radiance mosaics, using bands 8-7-5 displayed as R-G-B. (a) Mosaic centered at 91.8°E, 18.6°S. Black arrows point to likely chloride-bearing units mapped by *Osterloo et al.* [2010]. White arrows point to margin of material which is similar to unit 2 in morphology and thermophysical properties but does not exhibit a strong TES 507 cm^{-1} feature and thus was mapped as unit 1. This material may represent a modified version of unit 2. (b) THEMIS spectra from Figure 22a, compared with average unit spectra from Figure 3 and with TES surface types 1 and 2 [*Bandfield et al.*, 2000b].

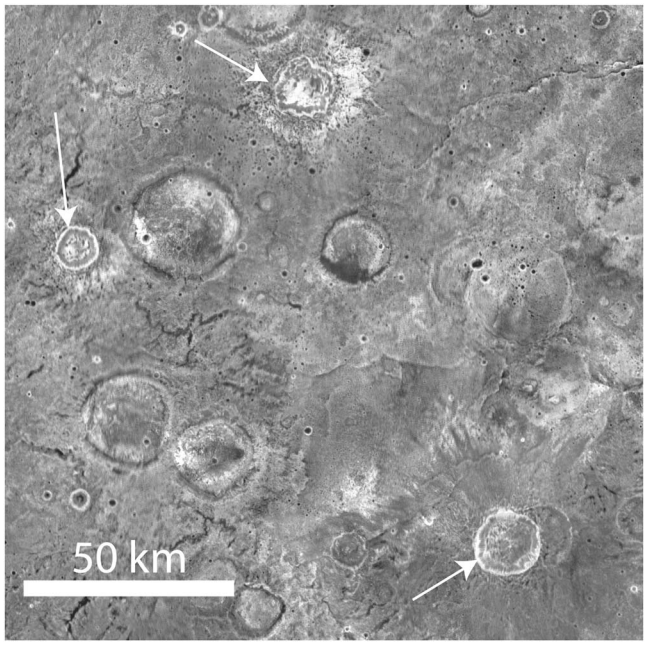

Figure 23. THEMIS nighttime IR radiance mosaic centered at 86.7°E, 9.5°S. Arrows point to craters with ejecta that show a thermal contrast from underlying target materials.

rims, and plains materials within the northern rim of Hellas Basin. These locations were also described by *Poulet et al.* [2005] and *Crown et al.* [2010]. Because the phyllosilicate minerals are associated with a variety of surfaces, and because only the lower resolution data were examined for this study (meaning, smaller detections might have been missed), it is difficult to draw meaningful implications about the origin of these minerals. Detailed, high-resolution studies of the individual phyllosilicate detections [e.g., *Seelos et al.*, 2010] are needed to better constrain their origin.

4. Discussion

4.1. Geologic Origins of Observed Units

4.1.1. Unit 1

[40] The degraded intercrater plains (unit 1) likely consist of a variety of materials including impact breccias, volcanic materials, and sediments [e.g., *Tanaka et al.*, 1988]. Based on superposition relationships, they are the oldest units in the region. However, the surface of the unit likely continues to be modified through aeolian, impact and possibly water-limited chemical alteration processes. The degraded plains units are likely altered to some degree, primarily on the basis of the presence of high-silica phases (~15%) [e.g., *Michalski et al.*, 2005], but also on the observation that the plains are heavily degraded, suggesting extensive mechanical and/or chemical processing that would likely lead to some degree of compositional modification (e.g., mineral-specific comminution [*Horz et al.*, 1984] or preferential mineral dissolution [*Tosca et al.*, 2004]). It is not clear whether the primary lithology of unit 1 was deficient in olivine (relative to unit 2) or whether olivine has been depleted through these later modification processes. This question is discussed in detail in section 4.4.

4.1.2. Unit 2

[41] Olivine-rich intercrater plains units (unit 2) are interpreted to be primarily volcanically emplaced, based on embayment relationships (Figure 6), large extent of individual occurrences (suggesting that an impact origin is unlikely), relatively resistant morphology and higher thermal inertia. The lack of a clear sedimentary source region for

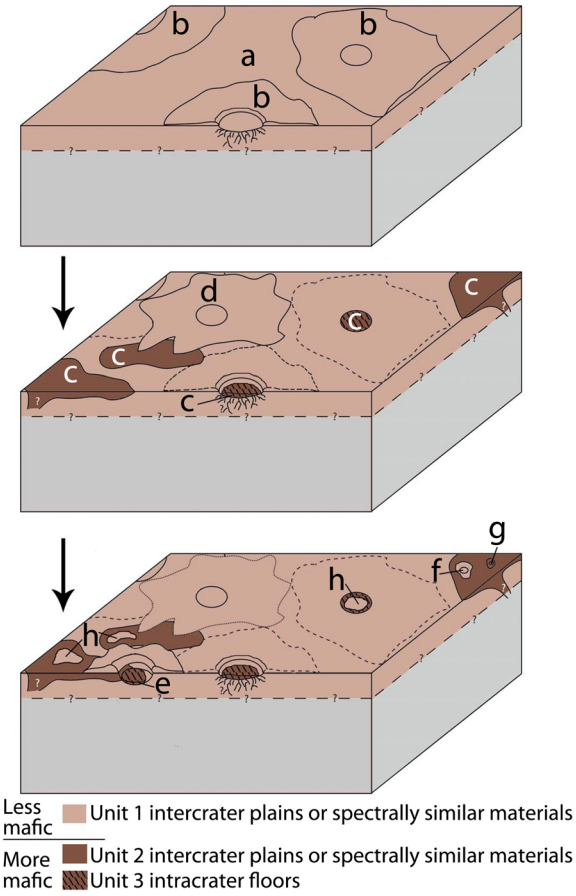

Figure 24. Cartoon depiction of the proposed sequence of events for units 1–3. The proposed sequence is as follows: Impacts (b) into ancient highlands surface (a) formed a cratered surface with intercrater plains. Portions of the intercrater plains and some crater floors are later resurfaced by volcanic infilling (c). These materials are enriched in olivine relative to the older units. It is unclear how much of the compositional difference between the two units is due to alteration of the older unit and how much is due to a primary difference in crust-forming magma compositions. During and after the emplacement of units 2 and 3, impacts continue to form crater ejecta (d) which partially bury the margins of older units. Some of these later impacts exposed unit 2 materials in the crater walls, which later eroded to partially fill some crater floors (e). Impacts into unit 2 excavate unit 1-like compositions from beneath (f); smaller impacts into unit 2 only expose unit 2 materials in their crater ejecta (g). Portions of unit 2 either are altered to become less mafic and similar to unit 1 or are covered with sediments derived with unit 1 (h). Unit 4 is a surficial unit only and therefore is not included in this diagram. The origin of unit 5 is poorly constrained and thus is also not included (see text).

the required volume of olivine-enriched sediment likely precludes a dominantly sedimentary origin, though it may explain some occurrences of this unit. The morphologic similarities between the various occurrences of unit 2 suggest that they were likely emplaced nearly contemporaneously, which would imply relatively widespread magmatism that postdates the formation of the primary crust. It is unclear how magma could be distributed over such a large area; however, widespread magmatism has been invoked for similar- or larger-sized areas for Hesperian ridged plains [*Head et al.*, 2002], formation of chaos terrain and Vallis Marineris troughs [e.g., *Sharp*, 1973; *Carr*, 1974; *Chapman and Tanaka*, 2002], and a probable exposed dike system over 600 km in length [*Head et al.*, 2006]. The heavily cratered nature of the crust in this region, including the Hellas impact basin, might have produced extensive subsurface fracture systems that intersect and perhaps enabled magma ascent.

4.1.3. Unit 3

[42] Resistant materials found on the floors of many craters (unit 3) are more difficult to interpret because of the geologic setting; the materials could represent volcanic infilling, lithified sediments, or perhaps impact melt and/or impact breccia. *McDowell and Hamilton* [2007] report observations of similar, resistant materials in Margaritifer Terra craters and evaluate the same three scenarios above. They rule out impact melt primarily on the basis of the depth of the crater floor relative to the crater diameters; the relationships suggest extensive infilling that likely would have buried any impact melt in the floor of the craters. In our study region, crater floors that host unit 3 are similarly shallow for their respective diameters (section 3.3), suggesting that impact melt and/or fallback breccia is an unlikely explanation. Sedimentary infill from surroundings is possible, but the composition is distinct from the surrounding dominant surface unit, unit 1. One would expect sediments to be primarily composed of the most areally abundant or most degraded surface unit (unit 1 in both cases), or at least be a mixture of the two most abundant surface units (units 1 and 2). Rather, the unit 3 crater floor interiors are spectrally indistinguishable from unit 2 and spectrally distinct from unit 1. The topographic characteristics of unit 3 surfaces (Figures 7 and 12) are puzzling. In some cases, the margins appear to conform to the lower portion of the crater wall (Figure 7). It is not clear what process could produce this topography. It is possible that the craters exposed unit 2-like material in the crater wall during impact, and that this material was then distributed across the floor via mass wasting and subsequently lithified. In one example shown in Figure 7, the steeper margin of unit 3 actually exhibits a lower thermal inertia than the floor; this observation might support the idea of continued erosion from the walls. But in most cases, the thermal inertia of the steep margin is higher than or similar to that of the floor. Alternatively, the unit 3 occurrences may have been originally flat-lying but experienced postdepositional modification such as erosion or subsidence. With subsidence, one might expect surface fracturing or a bench/terrace around the margin of unit 3. Bench-like features are observed in some cases; Figure 12 highlights one possible example. These features may also represent "high lava marks," which are sometimes observed at the margins of ponded lavas in lunar and Martian craters [e.g., *Greeley et al.*, 2005]. With the information available, it is difficult to favor erosion from the crater walls over volcanic infilling. Though there are no obvious lava flow features or source vents which would point to a volcanic origin, this is true for unit 2 as well, and it could be that these represent low-viscosity flood lavas that buried their vents, as suggested for some lunar craters and Gusev crater [e.g., *Greeley*, 1976; *Greeley et al.*, 2005]. Additionally, if unit 2 is volcanically emplaced via extensive subsurface fracturing, then presumably crater floors would also be overlying subsurface fracturing and would experience similar volcanic infilling.

4.1.4. Unit 4

[43] The TES and THEMIS spectral properties of the intracrater sand deposits (unit 4) suggest that sand deposits are intermediate between the olivine-enriched intercrater plains (unit 2) and olivine-deficient intercrater plains (unit 1), suggesting that they may be a mixture of the olivine-enriched and olivine-deficient plains materials. Alternatively, they may be less altered sediments from unit 1, where the mobile nature of the grains reduces preservation of evidence of surface alteration.

4.1.5. Unit 5

[44] Unit 5 is perhaps the most enigmatic of the units presented here. It is not associated consistently with any particular landform or spectral unit that might provide insight into its origin, and has a variable thermal inertia (Table 2). The margins of the unit are typically sharp: the THEMIS spectral signature changes from unit 5 to unit 1 or 2 over a distance of one or two THEMIS pixels (100–200 m) with no intermediate signature. This suggests that the unit is not particularly mobile, and may be directly tied to an underlying lithology or overlying unit that has been removed. The lack of a bedrock (defined as THEMIS thermal inertia >1200 J m^{-2} K^{-1} $s^{-1/2}$ [*Edwards et al.*, 2009]) source for this relatively isolated unit further suggests that it must be either mechanically or chemically derived from underlying material or from overlying material that has now been removed. Finally, small craters (<1 km) which impact into unit 5 commonly bear spectral resemblance to the underlying unit (Figure 1), suggesting that it does not have a substantial thickness.

[45] It is not clear if unit 5 represents a more altered or less altered version of associated units. For this discussion, it is important to note that determining which surface is more altered is not easily done on the basis of changes in primary mineral abundance alone (e.g., olivine, plagioclase, pyroxene). The relative stability of minerals, particularly plagioclase and pyroxene, in aqueous solution is highly dependent on solution pH and chemistry, the composition of the minerals (for example Ca-plagioclase is more susceptible to dissolution than pyroxene, which is more susceptible than Na-plagioclase), and the grain size of the mineral grains [e.g., *Keller*, 1955; *Loughnan*, 1969; *Schott and Berner*, 1985; *Hurowitz et al.*, 2005; *McAdam et al.*, 2006, 2008]. Furthermore, the nondetection of hydration signatures in CRISM data, which would be expected for some alteration minerals (e.g., clays, sulfates, amorphous/poorly crystalline silicates), is also not necessarily an indicator of lack of alteration. This is because poorly crystalline and/or amorphous hydrated silicates can lack 1.4 and 1.9 μm features that are associated with hydration in crystalline materials [*Milliken and Mustard*, 2005; *Kraft et al.*, 2007]. Additionally, in remotely sensed

data, the signature of weathering is commonly more affected by the differential breakdown of primary phases rather than the formation of secondary phases [*Michalski et al.*, 2005]. Thus, though the THEMIS signature of unit 5 suggests that it is more felsic/silicic than unit 1, this observation does not indicate that unit 5 is more altered than unit 1. With that in mind, one possible origin of unit 5 is that it represents less altered, fresher exposures of unit 1. The observations of unit 5 occurring on isolated buttes/massifs embayed by unit 2 (Figures 16 and 19) as well as on talus eroded from unit 1 (Figure 19) might suggest that perhaps some occurrences of unit 5 are more representative of the primary lithology of unit 1. Our logic here is that the same process that is keeping unit 2 relatively free of regionally derived, possibly altered sediment from unit 1 (based on the relatively higher thermal inertia of unit 2 in some areas) also keeps these isolated areas free of older, altered sediment from unit 1. Similarly, material eroded from quasi-vertical exposures of unit 1 (the talus slopes) likely are more representative of the volume of unit 1 than is the surface of unit 1.

[46] Conversely, unit 5 may represent a more altered end-member of unit 1, 2 or 3. If derived from underlying material, the enhanced alteration might have been enabled by underlying differences in primary lithology or grain/crystal size. Or, it may have experienced alteration at depth under unit 1, perhaps via groundwater or a local hydrothermal system, and has now been exposed in some places. Given the variability in morphologic associations, spectral unit associations, and thermal inertia, it is likely that separate occurrences of unit 5 may have had distinct formation mechanisms and/or multiple formation mechanisms.

4.1.6. Olivine- and Pyroxene-Rich Units

[47] Olivine and pyroxene-rich buttes, massifs and central peaks are mostly concentrated around the rim of Hellas Basin (Figures 16, 20, and 21) [*Poulet et al.*, 2007; *Koeppen and Hamilton*, 2008], suggesting that some are directly tied to the formation of Hellas Basin. It is possible that they represent mantle material that was brought close to the surface by the Hellas impact [e.g., *Koeppen and Hamilton*, 2008].

4.2. Proposed Sequence of Events

[48] In summary, we propose the following generalized geologic history of the region, which incorporates TES- and THEMIS-detected spectral units (Figure 24). Following formation of the earliest exposed crust, the surface was degraded via impact, aeolian, and/or fluvial processes,generating regolith from bedrock (unit 1) which may be indurated in some places. These processes may have resulted in mechanical and/or chemical alteration of the original surface composition; however, the original lithology (for example, the olivine content relative to younger units) is not well constrained.

[49] Later, widespread volcanism resulted in partial filling of intercrater plains (unit 2) and possibly crater floors (unit 3). Some impacts occurring during or after this time may have exposed unit 2-like materials in crater walls, which were then distributed across the crater floors. All three units (1, 2 and 3) continued to be reworked and resurfaced, resulting in partial burial of units 2 and 3 with locally derived sediment as well as older (and perhaps regionally derived) sediment from unit 1. Chloride deposits formed in association with unit 2-like surfaces after substantial modification (to reduce the strength of the TES 507 cm^{-1} index) and perhaps burial (Figure 22). The fraction of sediment most conducive to saltation then formed dunes and other bed forms (unit 4).

[50] The formation mechanism(s) of unit 5 is/are so ill-constrained that it is difficult to incorporate it into the sequence with any reasonable certainty. It may represent isolated areas that underwent additional chemical alteration to produce slightly more silicic/felsic surfaces. In this case, the enhanced alteration may have been enabled by underlying differences in primary lithology or grain size; or was perhaps assisted by local ground waters or hydrothermal systems and later exposed. Alternatively, it may represent a less altered version of unit 1 that has been exposed by erosion (section 4.1.5).

4.3. Relationship to Similar Units in Other Noachian Highlands Regions

[51] Units 1, 2, and 3 bear strong resemblance to units observed in Mare Serpentis, a low-albedo heavily cratered region northwest of Hellas Basin. *Rogers et al.* [2009] reported high thermal inertia, resistant mafic units interspersed throughout less mafic, lower thermal inertia degraded plains. They suggested that the mafic units likely represented volcanically emplaced materials that postdate older, less mafic plains units. As described here for unit 1, it is not clear if the primary lithology of the older units was originally less mafic or if the present-day olivine-deficient composition was achieved through alteration processes [*Rogers et al.*, 2009]. Similar to this study region, the resistant mafic materials in Mare Serpentis are also found in crater floors. The major difference between Mare Serpentis mafic units and units 2 and 3 from this study are the overall thermal inertia ranges; mafic units in Mare Serpentis reach thermal inertias as high as 500–1200 J m^{-2} K^{-1} $s^{-1/2}$, compared to a maximum of ~420 J m^{-2} K^{-1} $s^{-1/2}$ for this study region. The difference could simply be related to efficiency of sediment removal between the two regions; local wind patterns could facilitate increased areal coverage of sediment-free surfaces in Mare Serpentis.

[52] Elsewhere in the highlands, high thermal inertia, flat-floored craters have been examined in detail [*Mest and Crown*, 2005; *McDowell and Hamilton*, 2007; *Edwards et al.*, 2010]. In contrast with the unit 3 surfaces presented here, craters in Margaritifer Terra do not typically appear spectrally unique from surrounding materials in THEMIS data [*McDowell and Hamilton*, 2007]. However, preliminary examination of some of those craters using the 507 cm^{-1} index indicates that some may at least have spectral distinctions at long wavelengths in TES data. The geomorphology of Millochau Crater was examined in detail by *Mest and Crown* [2005]. The crater floor partially consists of similar material to unit 3 (mapped as "rugged material" by Mest and Crown); they report a gentle sloping from the edge of the rugged material downward toward the crater center, as observed here for some occurrences of unit 3. *Mest and Crown* [2005] suggest that the rugged material may consist in part of mass-wasting material, though they note that the absence of transverse ridges and other morphological features associated with gravity-driven flow are puzzling. They also suggest that the topographic characteristics are consistent with postmodification of near-horizontal strata.

The characteristics they describe are similar to our observations of unit 3. Preliminary work by *Edwards et al.* [2010] suggests that the relative increase of mafic minerals found in flat-floored high thermal inertia Intracrater deposits is a widespread trend throughout the highlands. They suggest that the crater filling process may have been dominated by impact-driven volcanism, such as that proposed for some lunar craters [*Schultz*, 1976].

[53] *Bandfield* [2008] described high-silica deposits in Hellas Basin, consisting of ~80% high-silica phases such as amorphous silica or zeolite; the identification was made using both THEMIS and TES data. Additionally, bright soils uncovered by the Mars Exploration Rover *Spirit* in Gusev Crater were found to consist of >80% SiO_2 [*Squyres et al.*, 2008]. Areas described as unit 5 differ from the Hellas deposits in both THEMIS and TES data. Unit 5 surfaces do not exhibit the low surface emissivity at ~8.5 μm (THEMIS band 4) nor the relatively featureless emissivity at wavelengths >~25 μm (<400 cm^{-1}) in TES data. Thus, although unit 5 is relatively silicic/felsic compared to unit 2, it is not similar to Hellas or Gusev soils, which are overwhelmingly dominated by silica.

4.4. Outstanding Questions Related to Major THEMIS Signatures in the Highlands

[54] Results from this work and other studies highlight a few outstanding questions regarding highland surface compositions, and in particular, regarding spectral unit signatures that are commonly observed in THEMIS data. The first question relates to the true composition of the heavily degraded unit 1. There are clearly two dominant spectral units in the intercrater plains, represented here as units 1 and 2 and by *Rogers et al.* [2009] as less mafic, low thermal inertia plains and mafic rocky surfaces. These differ from each other in relative age, composition, and thermophysical properties. It is not clear if the older, less mafic unit (unit 1 in this work) represents a truly different lithology from the younger units, or if the units were actually similar in composition, but the older unit has experienced more alteration. If unit 5 represents a less altered version of unit 1, then this would suggest that the primary lithology of unit 1 truly was and is olivine-deficient. *Rogers* [2011] reported that crater ejecta in this region commonly exhibit increased abundances of plagioclase and/or high-silica phases and decreased abundances of pyroxene, relative to the target materials. Rogers suggests, among other scenarios, that the craters are either exposing (1) more pristine or (2) more altered materials than the surrounding target surface. The increased abundance of high-silica phases in the ejecta materials, however, more strongly supports the latter scenario. The ejecta materials found within unit 1 are not deficient or enriched in olivine relative to unit 1, but are deficient relative to unit 2. If the craters are exposing more altered material, the implication is that the olivine abundance associated with unit 1 was likely higher at the time of crystallization, but has been decreased because of alteration. (Olivine is more susceptible to dissolution than pyroxene; thus if pyroxene is decreased because of alteration, then olivine would also have been decreased). However, the subsurface alteration scenario favored by *Rogers* [2011] depends heavily on the observation of slightly higher abundances of high-silica phases in ejecta materials, which could potentially represent glass or shocked materials instead of aqueous alteration phases. More importantly, the slight difference in high-silica abundance was not considered to be statistically separable for many of the craters examined [*Rogers*, 2011]. Thus, the possible clues from the crater ejecta are equivocal and the question remains: at the time of crystallization, were these older materials deficient in olivine relative to younger units?

[55] Answering this question has important implications for understanding the role of aqueous alteration in soil formation as well as the expected global volume of Mg-bearing alteration products. For example, *Bandfield et al.* [2011] recognize a global trend whereby rocky surfaces typically contain higher abundances of olivine than lower thermal inertia surfaces. They pose the hypothesis, drawing from geochemical observations in laboratory [e.g., *Tosca et al.*, 2004] and in situ Mars surface studies [*Hurowitz et al.*, 2006], that this trend can be explained by olivine dissolution by aqueous alteration during the formation of Martian soils from bedrock. In areas where olivine-deficient sediment can be clearly traced to olivine-rich bedrock (such as in Argyre Basin [*Bandfield and Rogers*, 2008]), the hypothesis is firmly supported. However, for much of the Martian surface, the source of soils is not well constrained. It is possible that the lower olivine abundance in most Martian soils (relative to younger bedrock) is due to derivation from older, olivine-deficient bedrock that has now been obscured by olivine-deficient regolith derived from that older bedrock. The olivine-enriched bedrock sources (units 2 and 3 in this work) cover a small area relative to olivine-deficient surfaces, thus one would expect olivine-deficient soils to be volumetrically dominant over olivine-enriched soils in any case. High abundances (>30%) of Mg sulfate are observed in strata in isolated areas on Mars [e.g., *McLennan et al.*, 2005; *Glotch et al.*, 2006] and could be ubiquitously present at lower abundances (5–10%, below the TES detection limit) in Martian soils [e.g., *Bandfield*, 2002; *Rogers and Aharonson*, 2008]. Additionally, Fe- and Mg-bearing clay minerals are some of the most commonly detected phyllosilicates to date in CRISM and OMEGA data [e.g., *Murchie et al.*, 2009; *Milliken and Bish*, 2010]. Dissolution of olivine is thought to be a primary source for the Mg cations needed to form these minerals [e.g., *Tosca et al.*, 2004; *Hurowitz et al.*, 2005]. Thus, determining the expected volume of Mg-bearing secondary minerals in Martian soils should depend on the starting compositions of ancient crustal materials. In summary, results from this and previous work demonstrate that the original olivine abundance of degraded intercrater plains surfaces is not well constrained. This question might potentially be addressed through detailed, systematic studies of exposed subsurface compositions in impact materials.

[56] A second question relates to the origin of less mafic material commonly observed overlying resistant olivine-enriched intercrater plains (e.g., Figure 1). In some cases, a strong thermal inertia distinction from unit 2 is not observed (Figure 1), whereas in other cases, the thermal inertia is decreased relative to unit 2 exposures, indicating variable thickness. We interpret this material as either sediment derived from unit 1, or material directly derived from alteration of the underlying unit 2. Distinguishing between these interpretations has important implications for the role

and timing of olivine alteration in Martian soils. For example, if the deposits are material directly altered from unit 2, then it implies that conditions conducive to olivine alteration continued at least until the early Hesperian (based on age estimates for Hesperian "smooth units," designated Hpl3 by *Greeley and Guest* [1987], which sometimes coincide with unit 2 occurrences). The alteration scenario would also raise the question of what property (e.g., grain size, porosity, lithology) of unit 2 is changing to enhance alteration where the overlying material is found.

[57] A third question relates to understanding the dominant origin of the high-thermal inertia, olivine-enriched crater floor materials (unit 3 in this work). As discussed by *Edwards et al.* [2009, 2010], high thermal inertia, flat-floored craters are widespread in the Martian highlands. In some cases, they are not compositionally distinct from the surrounding degraded plains materials [e.g., *McDowell and Hamilton*, 2007]. In other cases, they are distinctly enriched in olivine and are spectrally similar to olivine enriched intercrater plains [*Rogers et al.*, 2009; this work]. It is not clear if these differences are due to true lithologic differences between the deposits, or to differences in alteration/resurfacing between them. Furthermore, what is the origin of the crater filling material? As discussed by *McDowell and Hamilton* [2007] and in section 3.3, these crater floors are too shallow to represent impact melt/breccia material; this leaves volcanic and/or sedimentary interpretations. In the craters studied here, the compositional similarity to unit 2 argues against sedimentary infill from outside the crater (section 4.1.3); however, it is possible that impacts into olivine-enriched materials (like unit 2) could have exposed these materials in crater walls, which were then subsequently eroded and distributed across the floor of the crater. A volcanic origin also cannot be ruled out (section 4.1.3). Understanding the origin of these widespread materials has important implications for the volcanic and sedimentary history of Mars; namely, constraining the degree of and timing of volcanic resurfacing and/or sediment generation from unit 2-type surfaces.

[58] A fourth question relates to the dominant origin of unit 5 surfaces, which are spectrally distinct from the dominant unit in the region, unit 1, and are likely more felsic/silicic in composition than unit 1. The origin of these materials, and their relationship to other units, are poorly constrained. As discussed in section 4.1.5, they may represent altered versions of units 1 or 2, or, could represent less altered versions of unit 1. Distinguishing between these scenarios has important implications for the nature of the true composition of ancient crustal materials, and relates back to the first question above: were older unit 1 materials deficient in olivine at the time of crystallization? If unit 5 is representative of the true composition of unit 1, then it would suggest a true deficiency in olivine relative to younger units. If, on the other hand, unit 5 represents an altered version of unit 1, it may imply local groundwater or hydrothermal systems that led to enhanced alteration, then later exposure by erosion.

5. Conclusions

[59] Infrared observations in Tyrrhena and Iapygia Terrae (60–100°E, 0–30°S) illustrate an example of what may be typical southern highlands stratigraphy, including the presence of ancient, likely altered crust, overlain by relatively unaltered, intact lavas, both of which are interlayered with impact ejecta that derive material from depth (Figure 24). The observations may have more widespread implications for crustal evolution and alteration processes in the Martian highlands. The major observations, conclusions and unanswered questions are detailed below.

[60] 1. Intercrater plains can be divided into two main types: mafic, resistant, higher thermal inertia surfaces (unit 2) and less mafic, degraded, lower thermal inertia surfaces (unit 1). The more mafic units, which are likely volcanic in origin, overlie the less mafic units. These two units bear strong resemblance to intercrater plains units and stratigraphy found in Mare Serpentis, a low albedo highlands region located northwest of Hellas Basin. The widespread occurrence of unit 2-like surfaces call for its recognition as an important component of Mars' hjghland stratigraphy.

[61] Unit 1 is likely altered to some degree. However, a major outstanding question is whether the difference in olivine abundance between these two widespread units can be entirely attributed to alteration. It is possible that crust-forming materials that comprise the older unit, unit 1, were deficient in olivine at the time of crystallization. Answering this question has important implications for constraining the role of aqueous alteration in the formation in Martian regolith as well as for understanding possible changes in crust-forming magmas with time (section 4.4).

[62] 2. Isolated occurrences of olivine-deficient material are spectrally distinct from units 1–3, with a higher emissivity between 10.2 and 11.8 μm, suggesting a more felsic/silicic composition than units 1–3. These units are referred to as unit 5 in this work. The mineralogic distinction from unit 1 is unclear. The THEMIS signature could result from a slightly higher abundance of high-silica phases, which would likely indicate that unit 5 represents an altered version of units 1, 2 or 3. Alternatively, the signature could result from a higher plagioclase to pyroxene ratio relative to unit 1. Because mineral dissolution susceptibilities depend on a variety of factors, a higher plagioclase to pyroxene ratio in unit 5 could indicate either differential alteration of unit 1 to form unit 5, or conversely could indicate that unit 5 represents less altered exposures of the more widespread unit 1 (section 4.1.5). Thus, the origin of unit 5 materials is poorly constrained; they may represent less altered versions of unit 1 or more altered versions of units 1, 2 or 3. Understanding the origin(s) of this unit would provide insight into the question of whether unit 1 materials were olivine deficient at the time of crystallization (section 4.4).

[63] 3. Many craters in the region exhibit shallow interiors that are relatively high thermal inertia and compositionally indistinguishable from mafic intercrater plains surfaces (unit 2). These materials (unit 3) likely represent volcanic infill or sediment eroded from olivine-enriched materials (unit 2) exposed in crater walls. Because crater-fill materials similar to unit 3 are observed in many other highland locations (section 4.3), identifying the dominant origin of these materials would have important implications for the volcanic and sedimentary history of the highlands. In particular, it would provide constraints on the timing and degree of volcanic resurfacing and/or sediment generation from unit 2-type surfaces.

[64] In addition to the major conclusions described above, we also conclude the following:

[65] 4. A new TES spectral index (the "507 cm^{-1} index") is described. The index maps the strength of the emissivity slope between ~430 and ~508 cm^{-1} and is affected by the abundance of olivine and/or pyroxene on the surface, relative to plagioclase or high-silica phases. This index distinguishes unit 2 and unit 3 from unit 1 surfaces and was used to identify all occurrences of unit 2 and unit 3.

[66] 5. Olivine- and pyroxene-rich buttes, massifs and crater central peaks are observed in isolated locations near the southern portion of the study region, primarily concentrated on the rim of Hellas Basin. Many outcrops of these materials may have been brought near the surface via the Hellas impact.

[67] 6. Phyllosilicate-bearing surfaces are found in association with unit 1 or in crater-related materials (ejecta, walls, rims, central uplifts). No detections were found in association with the younger units 2–5; however, it is possible that some phyllosilicate-bearing surfaces might be found in these units if higher resolution targeted CRISM images are examined.

[68] 7. Putative chloride-bearing deposits (mapped by *Osterloo et al.* [2010]) are found in areas mapped as unit 1. However, for the majority of chloride occurrences, the unit 1 surfaces in which the chlorides are found bear strong resemblance to unit 2 surfaces in morphology and THEMIS DCS images. Thus, though the areas that contain putative chloride deposits lack a strong 507 cm^{-1} index value (and therefore were mapped as unit 1), it is possible that these areas are modified versions of unit 2. It is not clear if this is relevant to the formation of the chloride-bearing surfaces.

[69] 8. Intracrater sand deposits (unit 4) are compositionally similar to unit 2, and spectrally intermediate between units 1 and 2, suggesting that the observed bed forms contain a mixture of the two units.

[70] **Acknowledgments.** This work was supported by the NASA Mars Data Analysis Program grants NNX08AL10G (A. D. R.) and NNX07AN85G (R. L. F.) and by the NASA Planetary Geology and Geophysics Program. We are grateful to Joseph Michalski and an anonymous reviewer for highly useful reviews. Tim Glotch provided helpful comments. We thank Mikki Osterloo for sharing her global map of proposed chloride deposits. Finally, we thank the JMARS software developers, THEMIS engineers, mission planners, and data archivists, and CRISM multispectral summary image validation teams for straightforward and highly valuable products.

References

Baldridge, A. M. (2007), Thermal infrared spectral studies of sulfates and chlorides: Applications to salts on the Martian surface, thesis, 204 pp., Ariz. State Univ., Tempe.

Bandfield, J. L. (2002), Global mineral distributions on Mars, *J. Geophys. Res.*, *107*(E6), 5042, doi:10.1029/2001JE001510.

Bandfield, J. L. (2008), High-silica deposits of an aqueous origin in western Hellas Basin, Mars, *Geophys. Res. Lett.*, *35*, L12205, doi:10.1029/2008GL033807.

Bandfield, J. L., and A. D. Rogers (2008), Olivine dissolution by acidic fluids in Argyre Planitia, Mars: Evidence for a widespread process?, *Geology*, *36*, 579–582, doi:10.1130/G24724A.1.

Bandfield, J. L., P. R. Christensen, and M. D. Smith (2000a), Spectral data set factor analysis and end-member recovery: Application to analysis of Martian atmospheric particulates, *J. Geophys. Res.*, *105*, 9573–9587, doi:10.1029/1999JE001094.

Bandfield, J. L., V. E. Hamilton, and P. R. Christensen (2000b), A global view of Martian surface compositions from MGS-TES, *Science*, *287*, 1626–1630, doi:10.1126/science.287.5458.1626.

Bandfield, J. L., D. Rogers, M. D. Smith, and P. R. Christensen (2004), Atmospheric correction and surface spectral unit mapping using Thermal Emission Imaging System data, *J. Geophys. Res.*, *109*, E10008, doi:10.1029/2004JE002289.

Bandfield, J. L., A. D. Rogers, and C. S. Edwards (2011), The role of aqueous alteration in the formation of Martian soils, *Icarus*, *211*, 157–171, doi:10.1016/j.icarus.2010.08.028.

Bibring, J. P., et al. (2005), surface diversity as revealed by the OMEGA/Mars Express observations, *Science*, *307*, 1576–1581, doi:10.1126/science.1108806.

Carr, M. H. (1974), Tectonism and volcanism of Tharsis region Of Mars, *J. Geophys. Res.*, *79*, 3943–3949, doi:10.1029/JB079i026p03943.

Chapman, M. G., and K. L. Tanaka (2002), Related magma-ice interactions: Possible origins of chasmata, chaos, and surface materials in Xanthe, Margaritifer, and Meridiani Terrae, Mars, *Icarus*, *155*, 324–339, doi:10.1006/icar.2001.6735.

Christensen, P. R., J. L. Bandfield, V. E. Hamilton, D. A. Howard, M. D. Lane, J. L. Piatek, S. W. Ruff, and W. L. Stefanov (2000), A thermal emission spectral library of rock-forming minerals, *J. Geophys. Res.*, *105*, 9735–9739, doi:10.1029/1998JE000624.

Christensen, P. R., et al. (2001), Global Surveyor Thermal Emission Spectrometer experiment: Investigation description and surface science results, *J. Geophys. Res.*, *106*, 23,823–23,871, doi:10.1029/2000JE001370.

Christensen, P. R., et al. (2004), The Thermal Emission Imaging System (THEMIS) for the Mars 2001 Odyssey Mission, *Space Sci. Rev.*, *110*, 85–130, doi:10.1023/B:SPAC.0000021008.16305.94.

Christensen, P. R., J. L. Bandfield, R. L. Fergason, V. E. Hamilton, and A. D. Rogers (2008), The compositional diversity and physical properties mapped from the Mars Odyssey Thermal Emission Imaging System, in *The Martian Surface*, edited by J. F. I. Bell, pp. 221–241, Cambridge Univ. Press, New York, doi:10.1017/CBO9780511536076.011.

Crown, D. A., L. F. Bleamaster, S. C. Mest, J. F. Mustard, and M. Vincendon (2010), Geologic mapping of the NW rim of Hellas Basin, Mars: Evidence for an ancient buried landscape, *Lunar Planet. Sci.*, *41st*, Abstract 1888.

Edgett, K. S., and P. R. Christensen (1991), The particle size of Martian aeolian dunes, *J. Geophys. Res.*, *96*(E5), 22,765–22,776, doi:10.1029/91JE02412.

Edgett, K. S., and P. R. Christensen (1994), Mars aeolian sand: Regional variations among dark-hued crater floor features, *J. Geophys. Res.*, *99*(E1), 1997–2018, doi:10.1029/93JE03094.

Edwards, C. S., J. L. Bandfield, P. R. Christensen, and R. L. Fergason (2009), Global distribution of bedrock exposures on Mars using THEMIS high-resolution thermal inertia, *J. Geophys. Res.*, *114*, E11001, doi:10.1029/2009JE003363.

Edwards, C. S., J. L. Bandfield, D. Rogers, and P. R. Christensen (2010), Mafic high inertia crater floors in the southern highlands: Implications for a widespread post-impact modification process on Mars, Abstract P53C-1531 presented at 2010 Fall Meeting, AGU, San Francisco, Calif., 13–17 Dec.

Fenton, L. K., J. L. Bandfield, and A. W. Ward (2003), Aeolian processes in Proctor Crater on Mars: Sedimentary history as analyzed from multiple data sets, *J. Geophys. Res.*, *108*(E12), 5129, doi:10.1029/2002JE002015.

Fergason, R. L., P. R. Christensen, and H. H. Kieffer (2006a), High-resolution thermal inertia derived from the Thermal Emission Imaging System (THEMIS): Thermal model and applications, *J. Geophys. Res.*, *111*, E12004, doi:10.1029/2006JE002735.

Fergason, R. L., P. R. Christensen, J. F. Bell III, M. P. Golombek, K. E. Herkenhoff, and H. H. Kieffer (2006b), Physical properties of the mars Exploration Rover landing sites as inferred from Mini-TES-derived thermal inertia, *J. Geophys. Res.*, *111*, E02S21, doi:10.1029/2005JE002583.

French, B. M. (1998), *Traces of Catastrophe: A Handbook of Shock-Metamorphic Effects in Terrestrial Meteorite Impact Structures, LPI Contrib. 954*, 120 pp., Lunar and Planet. Inst., Houston, Tex.

Garvin, J. B., S. E. H. Sakimoto, and J. J. Frawley (2000), Geometric properties of Martian impact craters: An assessment from the Mars Orbiter Laser Altimeter (MOLA) digital elevation modes, *Lunar Planet Sci.*, *XXXI*, Abstract 1619.

Gillespie, A. R., A. B. Kahle, and R. E. Walker (1986), Color enhancement of highly correlated images. I. Decorrelation and HSI contrast stretches, *Remote Sens. Environ.*, *20*, 209–235, doi:10.1016/0034-4257(86)90044-1.

Glotch, T. D., R. V. Morris, P. R. Christensen, and T. G. Sharp (2004), Effect of precursor mineralogy on the thermal infrared emission spectra of hematite: Application to Martian hematite mineralization, *J. Geophys. Res.*, *109*, E07003, doi:10.1029/2003JE002224.

Glotch, T. D., J. L. Bandfield, P. R. Christensen, W. M. Calvin, S. M. McLennan, B. C. Clark, A. D. Rogers, and S. W. Squyres (2006), Min-

eralogy of the light-toned outcrop at Meridiani Planum as seen by the Miniature Thermal Emission Spectrometer and implications for its formation, *J. Geophys. Res.*, *111*, E12S03, doi:10.1029/2005JE002672.

Greeley, R. (1976), Modes of emplacement of basalt terrains and an analysis of mare volcanism in the Orientale Basin, *Proc. Lunar Sci. Conf.*, *7th*, 2747–2759.

Greeley, R., and J. E. Guest (1987), Geologic map of the eastern equatorial region of Mars, *U.S. Geol. Surv. Misc. Invest. Ser. Map*, *I-1802-B*.

Greeley, R., and B. D. Schneid (1991), Magma generation on Mars: Amounts, rates, and comparisons with Earth, Moon, And Venus, *Science*, *254*, 996–998, doi:10.1126/science.254.5034.996.

Greeley, R., B. H. Foing, H. Y. McSween Jr., G. Neukum, P. Pinet, M. van Kan, S. C. Werner, D. A. Williams, and T. E. Zegers (2005), Fluid lava flows in Gusev crater, Mars, *J. Geophys. Res.*, *110*, E05008, doi:10.1029/2005JE002401.

Head, J. W., III, M. A. Kreslavsky, and S. Pratt (2002), Northern lowlands of Mars: Evidence for widespread volcanic flooding and tectonic deformation in the Hesperian Period, *J. Geophys. Res.*, *107*(E1), 5003, doi:10.1029/2000JE001445.

Head, J. W., L. Wilson, J. Dickson, and G. Neukum (2006), The Huygens-Hellas giant dike system on Mars: Implications for Late Noachian-Early Hesperian volcanic resurfacing and climatic evolution, *Geology*, *34*, 285–288, doi:10.1130/G22163.1.

Horz, F., M. J. Cintala, T. H. See, F. Cardenas, and T. D. Thompson (1984), Grain-size evolution and fractionation trends in an experimental regolith, *J. Geophys. Res.*, *89*, C183–C196, doi:10.1029/JB089iS01p0C183.

Hurowitz, J. A., S. M. McLennan, D. H. Lindsley, and M. A. A. Schoonen (2005), Experimental epithermal alteration of synthetic Los Angeles meteorite: Implications for the origin of Martian soils and identification of hydrothermal sites on Mars, *J. Geophys. Res.*, *110*, E07002, doi:10.1029/2004JE002391.

Hurowitz, J. A., S. M. McLennan, N. J. Tosca, R. E. Arvidson, J. R. Michalski, D. W. Ming, C. Schröder, and S. W. Squyres (2006), In situ and experimental evidence for acidic weathering of rocks and soils on Mars, *J. Geophys. Res.*, *111*, E02S19, doi:10.1029/2005JE002515.

Jakosky, B. M. (1979), The effects of nonideal surfaces on the derived thermal properties of Mars, *J. Geophys. Res.*, *84*(B14), 8252–8262, doi:10.1029/JB084iB14p08252.

Jaumann, R., et al. (2007), The High-Resolution Stereo Camera (HRSC) experiment on Mars Express: Instrument aspects and experiment conduct from interplanetary cruise through the nominal mission, *Planet. Space Sci.*, *55*, 928–952, doi:10.1016/j.pss.2006.12.003.

Johnson, J. R., F. Hörz, P. G. Lucey, and P. R. Christensen (2002), Thermal infrared spectroscopy of experimentally shocked anorthosite and pyroxenite: Implications for remote sensing of Mars, *J. Geophys. Res.*, *107*(E10), 5073, doi:10.1029/2001JE001517.

Keller, W. D. (1955), *The Principles of Chemical Weathering*, 88 pp., Lucas Bros., Columbia, Mo.

Kieffer, H. H., S. C. Chase Jr., E. Miner, G. Münch, and G. Neugebauer (1973), Preliminary report on infrared radiometric measurements from the Mariner 9 spacecraft, *J. Geophys. Res.*, *78*(20), 4291–4312, doi:10.1029/JB078i020p04291.

Kieffer, H. H., T. Z. Martin, A. R. Peterfreund, B. M. Jakosky, E. D. Miner, and F. D. Palluconi (1977), Thermal and albedo mapping of Mars during the Viking primary mission, *J. Geophys. Res.*, *82*(28), 4249–4291, doi:10.1029/JS082i028p04249.

Koeppen, W. C., and V. E. Hamilton (2008), Global distribution, composition, and abundance of olivine on the surface of Mars from thermal infrared data, *J. Geophys. Res.*, *113*, E05001, doi:10.1029/2007JE002984.

Kraft, M. D., T. G. Sharp, J. R. Michalski, and E. B. Rampe (2007), Combined thermal and near infrared spectra of hydrous silica coatings: Implications for surface type 2 mineralogy and recent liquid water on Mars, *Lunar Planet. Sci.*, *XXXVIII*, Abstract 2241.

Loughnan, F. C. (1969), *Chemical Weathering of the Silicate Minerals*, Elsevier, New York.

Lyon, R. J. P. (1965), Analysis of rocks by spectral infrared emission (8 to 25 mMicrons), *Econ. Geol.*, *60*, 715–736, doi:10.2113/gsecongeo.60.4.715.

Malin, M. C. (1976), Nature and origin of intercrater plains on Mars in studies of the surface morphology of Mars, Ph.D. dissertation thesis, Calif. Inst. of Technol., Pasadena.

Malin, M. C., and K. S. Edgett (2001), Global Surveyor Mars Orbiter Camera: Interplanetary cruise through primary mission, *J. Geophys. Res.*, *106*, 23,429–23,570, doi:10.1029/2000JE001455.

Malin, M. C., et al. (2007), Context camera investigation on board the Mars Reconnaissance Orbiter, *J. Geophys. Res.*, *112*, E05S04, doi:10.1029/2006JE002808.

McAdam, A. C., M. Y. Zolotov, M. V. Mironenko, L. A. Leshin, and T. G. Sharp (2006), Aqueous chemical weathering of a Mars analog lithology: Kinetic modeling for a ferrar dolerite composition, *Lunar Planet. Sci.*, *XXXVII*.

McAdam, A. C., M. Y. Zolotov, T. G. Sharp, and L. A. Leshin (2008), Preferential low-pH dissolution of pyroxene in plagioclase-pyroxene mixtures: Implications for Martian surface materials, *Icarus*, *196*, 90–96, doi:10.1016/j.icarus.2008.01.008.

McDowell, M. L., and V. E. Hamilton (2007), Geologic characteristics of relatively high thermal inertia intracrater deposits in southwestern Margaritifer Terra, Mars, *J. Geophys. Res.*, *112*, E12001, doi:10.1029/2007JE002925.

McLennan, S. M., et al. (2005), Provenance and diagenesis of the evaporite-bearing Burns formation, Meridiani Planum, Mars, *Earth Planet. Sci. Lett.*, *240*, 95–121, doi:10.1016/j.epsl.2005.09.041.

Mest, S. C., and D. A. Crown (2005), Millochau crater, Mars: Infilling and erosion of an ancient highland impact crater, *Icarus*, *175*, 335–359, doi:10.1016/j.icarus.2004.12.008.

Michalski, J. R., M. D. Kraft, T. Diedrich, T. G. Sharp, and P. R. Christensen (2003), Thermal emission spectroscopy of the silica polymorphs and considerations for remote sensing of Mars, *Geophys. Res. Lett.*, *30*(19), 2008, doi:10.1029/2003GL018354.

Michalski, J. R., M. D. Kraft, T. G. Sharp, L. B. Williams, and P. R. Christensen (2005), Mineralogical constraints on the high-silica Martian surface component observed by TES, *Icarus*, *174*, 161–177, doi:10.1016/j.icarus.2004.10.022.

Michalski, J. R., M. D. Kraft, T. G. Sharp, L. B. Williams, and P. R. Christensen (2006), Emission spectroscopy of clay minerals and evidence for poorly crystalline aluminosilicates on Mars from Thermal Emission Spectrometer data, *J. Geophys. Res.*, *111*, E03004, doi:10.1029/2005JE002438.

Milliken, R. E., and D. L. Bish (2010), Sources and sinks of clay minerals on Mars, *Philos. Mag.*, *90*, 2293–2308, doi:10.1080/14786430903575132.

Milliken, R. E., and J. F. Mustard (2005), Quantifying absolute water content of minerals using near-infrared reflectance spectroscopy, *J. Geophys. Res.*, *110*, E12001, doi:10.1029/2005JE002534.

Murchie, S., et al. (2007), Compact reconnaissance Imaging Spectrometer for Mars (CRISM) on Mars Reconnaissance Orbiter (MRO), *J. Geophys. Res.*, *112*, E05S03, doi:10.1029/2006JE002682.

Murchie, S. L., et al. (2009), A synthesis of Martian aqueous mineralogy after 1 Mars year of observations from the Mars Reconnaissance Orbiter, *J. Geophys. Res.*, *114*, E00D06, doi:10.1029/2009JE003342.

Mustard, J. F., et al. (2008), Hydrated silicate minerals on mars observed by the Mars reconnaissance orbiter CRISM instrument, *Nature*, *454*, 305–309, doi:10.1038/nature07097.

Osterloo, M. M., V. E. Hamilton, J. L. Bandfield, T. D. Glotch, A. M. Baldridge, P. R. Christensen, L. L. Tornabene, and F. S. Anderson (2008), Chloride-bearing materials in the southern highlands of Mars, *Science*, *319*, 1651–1654, doi:10.1126/science.1150690.

Osterloo, M. M., F. S. Anderson, V. E. Hamilton, and B. M. Hynek (2010), Geologic context of proposed chloride-bearing materials on Mars, *J. Geophys. Res.*, *115*, E10012, doi:10.1029/2010JE003613.

Palluconi, F. D., and H. H. Kieffer (1981), Thermal inertia mapping of Mars from 60°S to 60°N, *Icarus*, *45*, 415–426, doi:10.1016/0019-1035(81)90044-0.

Poulet, F., J. P. Bibring, J. F. Mustard, A. Gendrin, N. Mangold, Y. Langevin, R. E. Arvidson, B. Gondet, and C. Gomez (2005), Phyllosilicates on Mars and implications for early Martian climate, *Nature*, *438*, 623–627, doi:10.1038/nature04274.

Poulet, F., C. Gomez, J. P. Bibring, Y. Langevin, B. Gondet, P. Pinet, G. Bellucci, and J. Mustard (2007), Martian surface mineralogy from Observatoire pour la Mineralogie, l'Eau, les Glaces et l'Activite on board the Mars Express spacecraft (OMEGA/MEx): Global mineral maps, *J. Geophys. Res.*, *112*, E08S02, doi:10.1029/2006JE002840.

Rogers, A. D. (2011), Crustal compositions exposed by impact craters in the Tyrrhena Terra region of Mars: Considerations for Noachian environments, *Earth Planet. Sci. Lett.*, *301*, 353–364, doi:10.1016/j.epsl.2010.11.020.

Rogers, A. D., and O. Aharonson (2008), Mineralogical composition of sands in Meridiani Planum determined from Mars Exploration Rover data and comparison to orbital measurements, *J. Geophys. Res.*, *113*, E06S14, doi:10.1029/2007JE002995.

Rogers, A. D., O. Aharonson, and J. L. Bandfield (2009), Geologic context of in situ rocky exposures in Mare Serpentis, Mars: Implications for crust and regolith evolution in the cratered highlands, *Icarus*, *200*, 446–462, doi:10.1016/j.icarus.2008.11.026.

Ruff, S. W. (2004), Spectral evidence for zeolite in the dust on Mars, *Icarus*, *168*, 131–143, doi:10.1016/j.icarus.2003.11.003.

Ruff, S. W., and P. R. Christensen (2002), Bright and dark regions on Mars: Particle size and mineralogical characteristics based on Thermal

Emission Spectrometer data, *J. Geophys. Res.*, *107*(E12), 5127, doi:10.1029/2001JE001580.

Ruff, S. W., and P. R. Christensen (2007), Basaltic andesite, altered basalt, and a TES-based search for smectite clay minerals on Mars, *Geophys. Res. Lett.*, *34*, L10204, doi:10.1029/2007GL029602.

Schott, J., and R. A. Berner (1985), Dissolution mechanisms of pyroxenes and olivines during weathering, in *The Chemistry of Weathering*, edited by J. I. Drever, pp. 35–54, D. Reidel, Boston, Mass.

Schultz, P. H. (1976), Floor-fractured lunar craters, *Moon*, *15*, 241–273, doi:10.1007/BF00562240.

Seelos, F. P., et al. (2007), CRISM Multispectral Survey Campaign: Status and initial mosaics, *Lunar Planet. Sci.*, *XXXVIII*, Abstract 2336.

Seelos, K. D., et al. (2010), Huygens crater and the highland terrains in western Tyrrhena Terra: Mineralogic mapping with CRISM data, *Lunar Planet Sci.*, *41st*, Abstract 2400.

Sharp, R. P. (1973), Mars: Troughed terrain, *J. Geophys. Res.*, *78*, 4063–4072, doi:10.1029/JB078i020p04063.

Smith, D. E., et al. (1999), The global topography of Mars and implications for surface evolution, *Science*, *284*, 1495–1503, doi:10.1126/science.284.5419.1495.

Smith, D. E., et al. (2001), Orbiter Laser Altimeter: Experiment summary after the first year of global mapping of Mars, *J. Geophys. Res.*, *106*, 23,689–23,722, doi:10.1029/2000JE001364.

Smith, M. D., J. L. Bandfield, and P. R. Christensen (2000), Separation of atmospheric and surface spectral features in Mars Global Surveyor Thermal Emission Spectrometer (TES) spectra, *J. Geophys. Res.*, *105*, 9589–9607, doi:10.1029/1999JE001105.

Smith, M. D., J. C. Pearl, B. J. Conrath, and P. R. Christensen (2001), One Martian year of atmospheric observations by the Thermal Emission Spectrometer, *Geophys. Res. Lett.*, *28*(22), 4263–4266, doi:10.1029/2001GL013608.

Squyres, S. W., et al. (2008), Detection of silica-rich deposits on Mars, *Science*, *320*, 1063–1067, doi:10.1126/science.1155429.

Tanaka, K. L., N. K. Isbell, D. H. Scott, R. Greeley, and J. E. Guest (1988), The resurfacing history of Mars: A synthesis of digitized, Viking-based geology, *Proc. Lunar Planet. Sci. Conf.*, *18th*, 665–678.

Tosca, N. J., S. M. McLennan, D. H. Lindsley, and M. A. A. Schoonen (2004), Acid-sulfate weathering of synthetic Martian basalt: The acid fog model revisited, *J. Geophys. Res.*, *109*, E05003, doi:10.1029/2003JE002218.

Williams, R. M. E., A. D. Rogers, M. Chojnacki, J. Boyce, K. D. Seelos, C. Hardgrove, and F. Chuang (2011), Evidence for episodic alluvial fan formation in far western Terra Tyrrhena, Mars, *Icarus*, *211*, 222–237, doi:10.1016/j.icarus.2010.10.001.

Wyatt, M. B., V. E. Hamilton, H. Y. McSween, P. R. Christensen, and L. A. Taylor (2001), Analysis of terrestrial and Martian volcanic compositions using thermal emission spectroscopy: 1. Determination of mineralogy, chemistry, and classification strategies, *J. Geophys. Res.*, *106*(E7), 14,711–14,732, doi:10.1029/2000JE001356.

Zuber, M. T., D. E. Smith, S. C. Solomon, D. O. Muhleman, J. W. Head, J. B. Garvin, J. B. Abshire, and J. L. Bufton (1992), The Mars Observer laser altimeter investigation, *J. Geophys. Res.*, *97*(E5), 7781–7797, doi:10.1029/92JE00341.

R. L. Fergason, Astrogeology Team, U.S. Geological Survey, 2255 N. Gemini Dr., Flagstaff, AZ 86001-1698, USA.

A. D. Rogers, Department of Geosciences, State University of New York at Stony Brook, 255 Earth and Space Sciences, Stony Brook, NY 11794-2100, USA. (adrogers@notes.cc.sunysb.edu)